Evolution of Extraframework Iron Species in Fe Silicalite

1. Effect of Fe Content, Activation Temperature, and Interaction with Redox Agents

G. Berlier,* G. Spoto,* S. Bordiga,* G. Ricchiardi,* P. Fisicaro,* A. Zecchina,*,[1] I. Rossetti,† E. Selli,†
L. Forni,† E. Giamello,‡ and C. Lamberti‡

*Dipartimento di Chimica Inorganica, Fisica e dei Materiali, Università di Torino, via P. Giuria, 7, I-10125 Torino, Italy; †Dipartimento di Chimica
Fisica ed Elettrochimica, Università di Milano, via C. Golgi, 19, I-20133 Milano, Italy; and ‡Dipartimento di Chimica Inorganica,
Fisica e dei Materiali, Università di Torino, via P. Giuria, 7, and INFM UdR di Torino Università, I-10125 Torino, Italy

A study was made of the iron species dislodged from the tetrahedral lattice position by thermal treatments in four Fe silicalite samples with Si/Fe ratios of 25, 50, 90, and 150. The last two samples have a sufficiently low iron concentration to be considered *true catalysts* (i.e., having Fe dilutions as low as that used in the industrial conversion of benzene to phenol (Si/Fe > 80)) in partial oxidation reactions. A systematic spectroscopic study is presented in order to obtain a global picture of a system whose complexity can be understood by assuming the formation of a wide variety of transient coordinatively unsaturated iron species, with different oxidation states, which ultimately lead to grafted or anchored isolated and/or clustered species by interaction with residual tetrahedral Si(OH)Fe, defective SiOH groups, or strained SiOSi bridges of the hosting matrix. The structure characterization was obtained by means of the parallel use of IR, X-ray absorption near-edge spectroscopy, and electron paramagnetic resonance techniques, before, during, and after interaction with CO, N_2O, and NO probe molecules. This approach was applied to samples characterized by different iron content, activation temperature, and redox treatments. This allowed us to throw light onto structure, oxidation state, and mutual interconversion of a very complex family of extraframework iron species. Oxidation with O_2 or N_2O led to the formation of strongly bonded oxygen species. The relation between these species and the so-called α-oxygen species, claimed as the active sites for the hydroxylation of benzene to phenol by N_2O, is discussed. © 2002 Elsevier Science (USA)

Key Words: Fe silicalite; extraframework iron; benzene hydroxylation.

1. INTRODUCTION

It is well known that the addition of trivalent heteroatoms, like Al, Ga, or Fe (1, 2), in the crystalline framework of MFI silicalite leads to the appearance of strong Brønsted sites, responsible for the activity of these materials in acid-catalyzed reactions. Migration of heteroatoms to extraframework positions, induced by thermal treatment, leads to the appearance of Lewis sites (3). As a consequence, after thermal treatment the solid can possess both types of acid sites, working separately or in a synergistic way. However, unlike Al, and to a lesser extent Ga, Fe can show different valence states (Fe^{2+}, Fe^{3+}, and even Fe^{4+}), depending on the reducing or oxidizing character of the reactants present in the catalyst environment, and hence can show redox properties. An important example of catalytic activity, associated with this interplay between different oxidation states of Fe (in partial or total extraframework positions), is the one-step oxidation of benzene to phenol using N_2O as oxidant (4, 5). Indeed, the selective addition of an oxygen atom into an aromatic C–H bond to yield phenols and naphthols is a very promising tool for the chemical industry, because the commonly employed route *via* the three-step cumene process is of great technological complexity.

Due to the high industrial interest of this process, a remarkable number of scientific studies have appeared concerning iron-containing MFI systems. Two main preparation procedures were employed to disperse iron species inside the zeolite channels: (i) postsynthesis addition via ion exchange in solution and in the gas phase (6–13) and (ii) controlled migration of iron into extraframework positions starting from MFI containing isomorphous Fe^{3+} (2, 14–19). Until now only the Fe-based systems prepared following the second method have been shown to possess sufficient stability and selectivity to be proposed as catalysts in partial oxidation reactions of industrial interest.

As far as the former method is concerned, which gives only Fe species in extraframework positions, there is an intrinsic difficulty in trying to achieve a "proper" cation exchange of di- or even trivalent ions inside high Si/Al ratio zeolite, such as ZSM-5. The simple exchange of $2X^+$ or $3X^+$ ions ($X = $ H or Na) with a Fe^{2+} or a Fe^{3+} ion is unlikely and more complex exchange processes must be invoked, which necessarily involve oxocations $(Fe_iO_j)^{n+}$

64

or hydroxocations $[Fe_i(OH)_j]^{n+}$. Of course, these species can undergo complex chemical transformations upon successive thermal treatments. Therefore it is clear that these processes yield overexchanged samples which, although possessing interesting activity in the selective catalytic reduction of NO_x (6, 11), are highly heterogeneous. Moreover, this procedure does not guarantee that the extraframework species are mainly located in the zeolitic channels and cavities. In particular the presence of Fe species located on the external surface cannot easily be ruled out, especially in samples exchanged via the gas phase. All these facts can, at least partially, explain the lack of reproducibility of the results related to samples prepared via the cation exchange methods (6–12).

Conversely, the preparation of Fe-based catalysts, starting from Fe-MFI samples exhibiting unique tetrahedral and isolated iron species, seems to represent a simpler and more reproducible way to disperse iron species into microporous matrices (2, 14–19). The isomorphous substitution method, although not allowing addition of a high percentage of iron, guarantees rather good dispersion. As the thermal treatments cause migration of Fe from framework to partial or total extraframework positions, also in this case we deal with catalysts with considerable complexity. Among the starting Fe-MFI samples, one should distinguish Fe–ZSM-5 from Fe silicalite. The former contains Si, Al, and Fe atoms in T positions, while the latter has only Si and Fe atoms. Due to the much higher stability of the Al atom in the MFI framework, Fe–ZSM-5 always shows a greater number of Brønsted sites than a similar Fe silicalite which has undergone the same thermal treatment. This observation has led some authors to hypothesize that Al(OH)Si Brønsted sites can also play a nonnegligible role in partial oxidation reactions (20, 21). Other authors claimed that the fundamental role is played by iron species (7, 14). Supporting this thesis is the evidence that Al-free Fe silicalite is active in partial oxidation reactions, while Fe-free ZSM-5 is not. For these reasons, it is evident that the understanding of the structure of the active centers and of the mechanism of partial oxidation reactions is vitally dependent upon the elucidation of such factors as (i) the number, the structure, the oxidation state, and the nuclearity of the extraframework sites; (ii) the effect of the Fe and Al concentration on cluster nuclearity; (iii) the role of thermal treatments in determining the site structure and location; and (iv) the propensity of the Fe sites to undergo redox processes.

Due to the complexity of the system, in this work we present an exhaustive characterization study with many complementary techniques of iron species formed inside MFI channels upon migration of Fe in a series of Fe silicalite samples with different iron content and subjected to different treatments. Particular attention is devoted to the changes of oxidation state of the Fe species upon thermal treatments and after interaction with NO, O_2, N_2O, H_2, and H_2O by employing the IR spectroscopy of adsorbed molecules. Nitric oxide was preferentially used as a molecular probe due to its strong affinity toward Fe, and because of the high intensity of the ν_{NO} bands (18, 22–26). A systematic investigation of the spectra of adsorbed NO as a function of iron concentration, activation time, temperature, and redox treatments was performed with the hope of understanding the complex mutual transformations of iron species. Similarly, the parallel evolution of X-ray absorption near-edge spectroscopy (XANES) and electron paramagnetic resonance (EPR) was followed.

2. EXPERIMENTAL

Four different Fe silicalite catalysts, characterized by a Si/Fe ratio of 25, 50, 90, and 150 (hereafter referred to as FeS25, FeS50, FeS90, and FeS150, respectively) were studied. Samples FeS25, FeS50, and FeS150 were prepared following the method of Szostak *et al.* (27), while for FeS90 the hydrothermal method described by Ratnasamy and Kumar (28) was adopted. All catalysts were separately washed, dried, and calcined in air at 823 K. The sample characterization has been performed on the calcined sample subsequently activated at 773, 973, or 1073 K *in vacuo*. Subsequently, the oxidative/reductive treatments were performed on the activated samples upon interaction with the oxidizing/reducing atmosphere for 1 h (temperature of contact is specified for each experiment in the results section).

X-band EPR spectra were collected at liquid nitrogen temperature on a Bruker EMX instrument always employing the same set of instrumental parameters. The sample was contained in a quartz cell designed to allow *in situ* thermal treatments and spectra recording.

The IR experiments were carried out on a Bruker IFS 66 FTIR instrument equipped with a cryogenic MCT detector and running at 2 cm^{-1} resolution. The samples were in the form of self-supporting pellets suitable for measurement in transmission mode. Measurement cells were used, allowing *in situ* thermal treatments (*in vacuo*, with reductive or oxidative agents) and dosing of probe molecules. CO ($P_{CO} = 20$ Torr) was dosed at liquid nitrogen temperature and successive IR spectra were collected upon reducing P_{CO}. N_2O ($P_{N_2O} = 15$ Torr) was dosed at room temperature and successive IR spectra were collected upon reducing P_{N_2O}. NO, carefully purified by distillation in order to remove other undesired nitrogen oxides ($P_{NO} = 15$ Torr), was dosed at room temperature: successive IR spectra have followed the system's evolution up to equilibrium, typically reached within 1 h. The successive evolution of spectra upon reducing P_{NO} was then followed. The last spectrum typically corresponds to 15 min of outgassing at room temperature (residual pressure lower than 10^{-3} Torr). In all experiments, the IR spectrum collected before gas dosage was used as background. All reported spectra are background-subtracted.

The X-ray absorption experiment was performed in transmission mode at the GILDA MB8 beamline at the European Synchrotron Radiation Facility. The monochromator was equipped with two Si(311) crystals while harmonic rejection was achieved using mirrors. For each spectrum an Fe metal foil spectrum was simultaneously collected using an I_2 detector. In order to ensure very-high-quality XANES spectra, the geometry of the beamline was optimized to improve the energy resolution: vertical slits, located 23 m from the source, were set to 0.6 mm, ensuring, at 7 keV, an actual energy resolution better than 0.4 eV. A sampling step of 0.2 eV for the XANES part of the spectra and a variable sampling step, giving $\Delta k_{max} = 0.05$ Å^{-1} for the EXAFS part and an integration time of 3 s/point, were adopted. Spectra were collected at room temperature using a metallic cell allowing *in situ* thermal treatments and gas dosage. For each sample three equivalent EXAFS spectra were collected, and the extracted $\chi(k)$ were averaged before the EXAFS data analysis. The EXAFS data analysis was performed following standard procedures (29). The first shell-filtered contribution was analyzed using the programs developed by Michalowicz (30). The EXAFS results were obtained using McKale phase and amplitude functions (31).

3. RESULTS

3.1. EXAFS Spectroscopy: The Effect of Thermal Treatments

Figure 1a reports the k^3-weighted, phase-uncorrected, FT of the EXAFS function of FeS90 catalyst in the presence of a template (full line curve) and after template removal and subsequent activation at 773 and 973 K (dotted and dashed curves, respectively). A dramatic reduction of the signal upon activation is observed. A quantitative EXAFS analysis was done only on the data obtained before template removal. This fit (Fig. 1b) yields to 3.8 ± 0.4 oxygen atoms located at 1.86 ± 0.01 Å.

3.2. High-Resolution XANES Spectroscopy: The Effect of Thermal Treatments and of Oxidation with N_2O

Figure 2a reports the XANES spectra of four model compounds of iron in different oxidation and coordination states: FePO$_4$ (Fe^{3+} in tetrahedral coordination), α-Fe$_2$O$_3$, and Fe(acac)$_3$ (Fe^{3+} in octahedral symmetry), and FeCp$_2$ as an example of Fe^{2+} compound (Cp = cyclopentadienyl, acac = acetylacetonate). The three ferric compounds exhibit the K-edge at higher energy (7122.5–7123.4 eV) than FeCp$_2$ (7119.4 eV). The $1s \rightarrow 3d$ preedge peak for FePO$_4$ (Fe^{3+} in tetrahedral coordination) is a relatively intense signal at 7114 eV (due to the $3p/3d$ mixing) (49), while for Fe^{3+} in octahedral symmetry, we observe two less intense components at the same energy. This signal is found at lower energy (7112.5 eV) for the ferrous FeCp$_2$ compound. A fi-
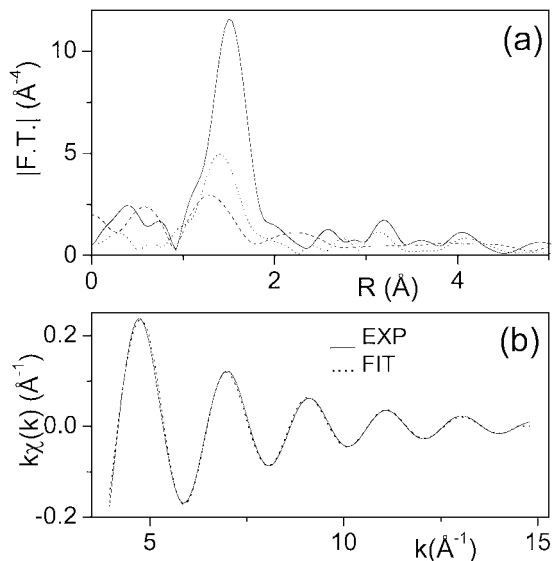

FIG. 1. (a) k^3-weighted, phase-uncorrected FT of sample FeS90 in the presence of template (full line) and after activation at 773 (dotted line) and 973 K (dashed line). (b) First shell-filtered $k\chi(k)$ function and corresponding best fit modeled with Fe–O contributions for FeS90 in the presence of template.

nal interesting feature of the XANES spectra reported in Fig. 2a is the intensity of the "white" line. Table 1 summarizes all the quantitative results extracted from the XANES spectra.

Figure 2b reports the spectra of FeS90 containing the template and after thermal treatments at increasing

TABLE 1

Position and Normalized Intensity of the 1s $\rightarrow$ 3d Preedge Peak and of the White Line of the XANES Spectra Reported in Fig. 2 for the Different Model Compounds and for FeS90 after Different Treatments[a]

Sample	Preedge peak		White line	
	Position (eV)	Intensity	Position (eV)	Intensity
FePO$_4$	7114.2	0.133	7136	1.35
Fe$_2$O$_3$	7113.4 (s)	0.056	7133.7	1.52
	7114.6	0.080		
Fe(acac)$_3$	7113.5 (s)	0.048	7132.5	1.60
	7114.6	0.053		
FeCp$_2$	7112.5	0.050	7133.7	1.52
FeS90[b]	7114.2	0.205	7138.1	1.31
FeS90[c]	7114.5	0.142	7136.7	1.23
FeS90[d]	7111.8 (s)	0.037	7136.7	1.20
	7114.5	0.128		
FeS90[e]	7114.3	0.137	7137.6	1.24

[a] s, Shoulder. The edge of the $1s \rightarrow 3d$ peak of Fe metal foil (defined at the inflection point) was set to be 7111.6 eV.
[b] With template.
[c] Activated at 773 K.
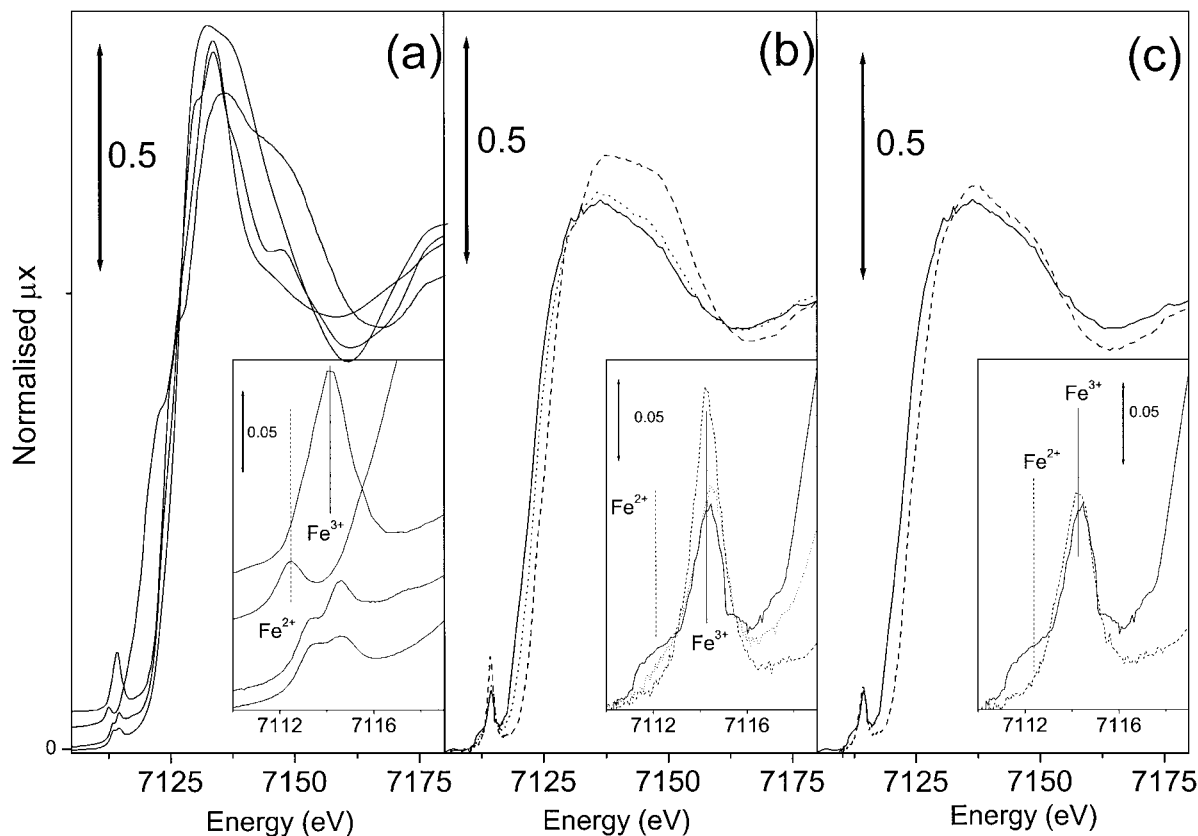[d] Activated at 973 K.
[e] After subsequent oxidation with N_2O at 523 K.

FIG. 2. (a) XANES spectra of model compounds. From top to bottom: $FePO_4$, $FeCp_2$, Fe_2O_3, and $Fe(acac)_3$ (Cp = cyclopentadienyl, acac = acetylacetonate). The four spectra were vertically shifted for clarity. (b) XANES spectra of FeS90 with template (dashed line) and activated at 773 (dotted line) and 973 K (solid line). (c) XANES spectra of FeS90 activated at 973 K (solid line, same curve as in part b, here reported again for direct comparison) and successively oxidized in N_2O at 523 K (dashed line). The insets of each part show the magnification of the preedge peak.

temperatures. The first effect of the thermal treatments is the shift of the K-edge position: from 7123.6 eV for the sample measured with template to 7122.4 and 7120.6 eV for the samples activated at 773 and 973 K, respectively. As a second effect, we observe a reduction of the $1s \rightarrow 3d$ peak intensity, with the simultaneous appearance of a low energy shoulder (around 7111.8 eV) whose intensity progressively increases with increasing activation temperatures.

We also notice that the sample with the template shows a white line intensity similar to that of $FePO_4$ (1.31 vs 1.35, see Table 1), i.e., much lower than that observed for sixfold coordinated model compounds (from 1.52 to 1.60). Activation at increasing temperatures causes a progressive reduction in white line intensity.

The effect of a successive oxidation treatment with N_2O is reported in Fig. 2c for the sample previously activated at 973 K. Oxidation causes the shift of the edge position from 7120.6 back to 7123.1 eV. Simultaneously, we observe the total erosion of the 7111.8 eV component of the $1s \rightarrow 3d$ preedge peak (see inset). A similar trend was observed with the sample activated at 773 K. Finally, we observe that the oxidation process causes the increase in the white line (Fig. 2c and Table 1).

The effect of oxidation has also been documented by EXAFS spectroscopy, as shown in Fig. 3, where the k^3-weighted, phase-uncorrected, FT of the EXAFS spectra collected on the FeS90 sample activated at 773 K are reported before and after oxidation with N_2O. Upon oxidation, a macroscopic variation of the first shell signal is observed: R goes from 1.40 to 1.34 Å and the corresponding maximum from 4.95 to 6.11 $Å^{-4}$.

3.3. IR Spectra of CO and N_2O Adsorbed on Activated, Oxidized, and Reduced Samples

The adsorption of CO and N_2O has been studied on the whole series of samples with Si/Fe content in the interval 25–150, after activation *in vacuo* at 773, 973, and 1073 K, and after oxidative (with O_2 and N_2O) and reductive (with H_2) treatments. For the sake of brevity we only report the results obtained upon adsorption of CO at 77 K on the most diluted sample FeS150 activated at 973 K.

The IR spectra of decreasing doses of CO on the sample activated *in vacuo* at 973 K are shown in Fig. 4a. By passing from the most intense spectrum (maximum coverage) to the less intense ($\theta \rightarrow 0$), we notice that the
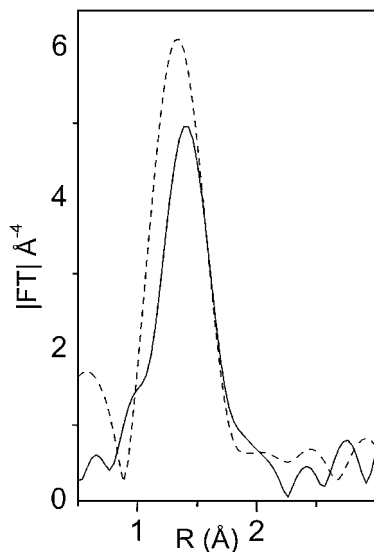
FIG. 3. k^3-weighted, phase-uncorrected, FT of the EXAFS function of catalyst FeS90 activated at 773 K before (solid line) and after (dashed line) oxidation in N_2O at 523 K.

strong band at 2138 cm^{-1} disappears first, followed by the composite absorption centered at 2173 cm^{-1} (with a shoulder at around 2162 cm^{-1}). The weaker absorption at 2215 cm^{-1} belongs to the most strongly adsorbed species, as it is the last to disappear upon CO desorption. The intensities of the whole bands depend upon the redox conditions: after oxidation with O_2 at 523 K (Fig. 4b) both the bands at 2215 and the composite adsorption at 2173 cm^{-1} are strongly depressed. After reduction with H_2 at 573 K (Fig. 4c) only the adsorption at 2215 cm^{-1} is drastically re-

FIG. 5. IR spectra of N_2O dosed at room temperature (decreasing P_{N_2O} from 15 to 10^{-3} Torr, solid-line spectra) on sample FeS50 after activation at 973 K. The dotted-line spectrum was obtained after adsorption at room temperature of $P_{N_2O} = 15$ Torr on a silicalite sample.

duced. Finally, the inset of Fig. 4 reports the O–H stretching bands before interaction with CO. It is important to notice the near total absence of the 3630 cm^{-1} band associated with the O–H stretching of the Si(OH)Fe groups (32).

As far as the spectra of N_2O are concerned, we only report (Fig. 5) the N–N stretching region of decreasing
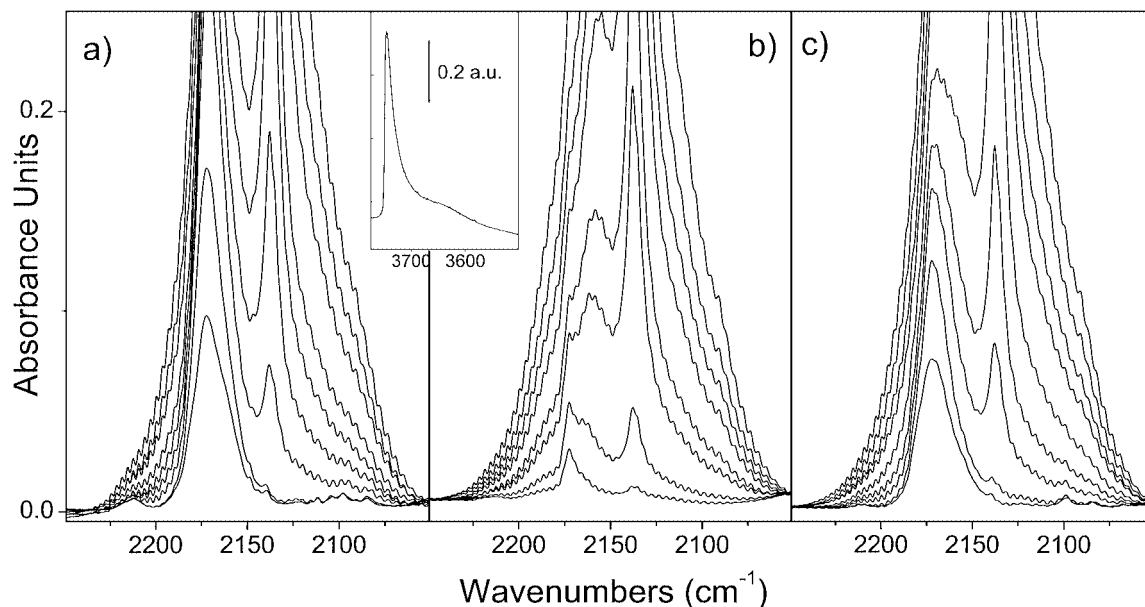

FIG. 4. IR spectra of CO dosed at 77 K (decreasing P_{CO}) on sample FeS150 after activation at 973 K (a), subsequent oxidation with O_2 at 523 K (b), and reduction with H_2 at 573 K (c). The inset shows experiment (a) monitored in the O–H stretching region before interaction with CO.
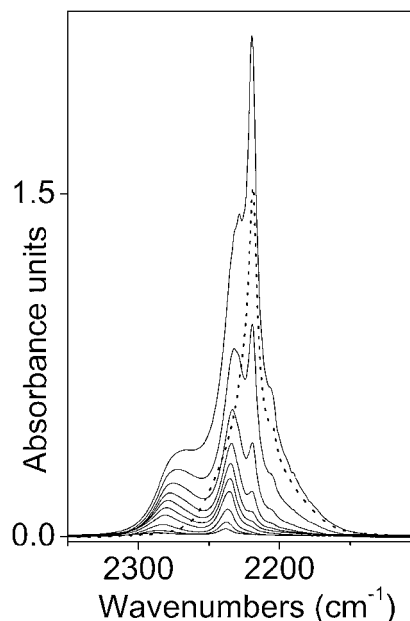
doses of N_2O adsorbed at room temperature on sample FeS50 outgassed at 973 K. Adsorption of N_2O is associated with the formation of three bands at 2275, 2235, and 2218 cm^{-1}. The dotted spectrum (characterized by one intense band around 2218 cm^{-1}) is due to N_2O adsorbed on silicalite and it is important for comparison. Both CO and N_2O IR spectra do not show any evolution with contact time.

3.4. IR Spectra of Adsorbed NO

Due to its strong affinity toward Fe, and because of the high intensity of the ν_{NO} bands (18, 22–26), the NO molecule is a very sensitive probe for the study of the oxidation and coordination state of iron in Fe silicalite. We thus report a detailed and systematic investigation of the spectra of adsorbed NO as a function of iron concentration, activation time, contact time, activation temperature, water preadsorption, redox treatments, and heating in NO.

3.4.1. The effect of Fe concentration. For simplicity, we illustrate only the effect, on the NO spectra, of iron concentration for samples outgassed *in vacuo* for 2 h at 773 K. Figure 6 illustrates the evolution upon P_{NO} of the IR spectra of adsorbed NO on all samples. The experiments were performed as follows: 15 Torr of NO were dosed on the sample and left to stand at room temperature for 1 h before recording the first spectrum. The coverage was then gradually decreased by lowering P_{NO}.

The first observation is that the overall integrated intensity of the IR bands increases with Fe concentration. However, this increase is not linear, particularly not when going from FeS50 to FeS25 (Figs. 6c and 6d). The second observation is that all spectra essentially consist of four bands coupled in two pairs. The first pair (1916, 1810 cm^{-1}) decreases simultaneously with P_{NO}, while the second pair (1835, 1765 cm^{-1}) behaves in the opposite way. Two isosbestic points are present, at 1830 and 1775 cm^{-1}. The intensity decrease in the 1810 cm^{-1} band (ΔI_{1810}) correlates linearly with ΔI_{1916}, as can be seen in the inset of Fig. 6a. Furthermore, a linear correlation is present between ΔI_{1810} and the increase in the band at 1765 cm^{-1} upon P_{NO} reduction (inset Fig. 6b).

3.4.2. The effect of activation time. To witness the role played by the duration of the thermal treatments, Fig. 7 reports the IR spectra registered immediately after NO dosage on sample FeS50 activated at 773 K for 1 h (instead of 2 h). After short activation, the IR spectra of adsorbed NO look markedly different, as can be seen by comparing Figs. 7 and 6c. The main difference is represented by the weaker intensity of the four bands, at 1916, 1810, and 1765 cm^{-1}, and by the presence of a new doublet centered around 1900 cm^{-1}. Notice that the doublet around 1900 cm^{-1} is absent on samples previously reduced with H_2 (see inset). Similar results have been obtained on the other samples and are not illustrated, for brevity.
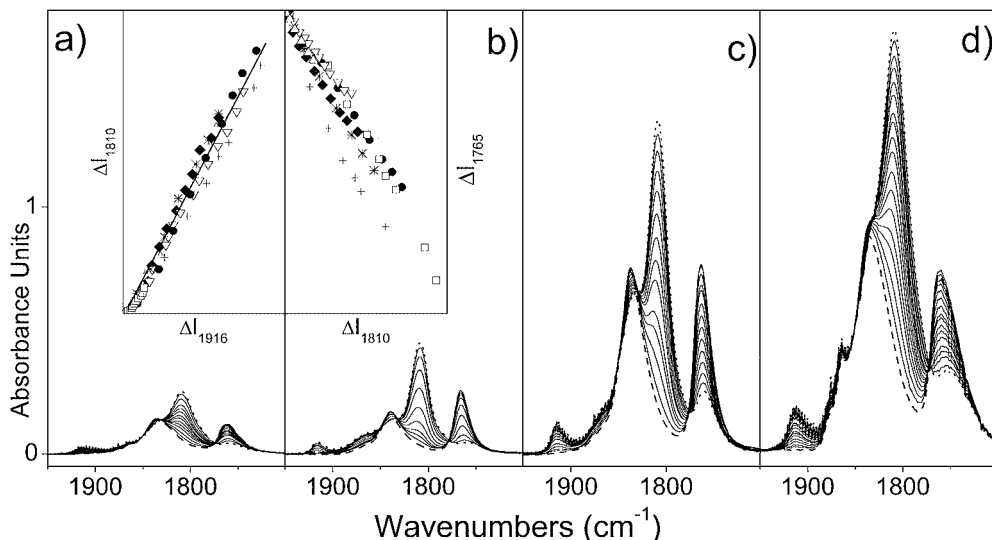
FIG. 6. IR spectra of NO dosed at room temperature (decreasing P_{NO} from 15 Torr, dotted-line spectrum, to 10^{-3} Torr, dashed-line spectrum) on samples FeS150 (a), FeS90 (b), FeS50 (c), and FeS25 (d) after activation at 773 K for 2 h. For the whole set of data, FeS150, □; FeS90, △; FeS50, ◆; FeS25, ▽. The relative intensity variation (ΔI_{1810}) measured between the first and the successive spectra of the band at 1810 cm^{-1} is reported in the inset of part a versus the same quantity measured for the 1916-cm^{-1} band (ΔI_{1916}). The linearity of the data indicates that the two bands are IR manifestations of the same species. The same quantity measured for the 1765-cm^{-1} band (ΔI_{1765}) is shown vs ΔI_{1810} in the inset of part b; in this case negatives values of ΔI_{1765} indicate an increase in this curve with decreasing P_{NO}. The reported linear relationships are general since they hold for all measured samples. Both insets report also the data coming from other experiments (FeS50 after H_2O absorption, +; FeS90 after steaming, ✳; FeS90 after steaming and treatment with dithionite, ●).
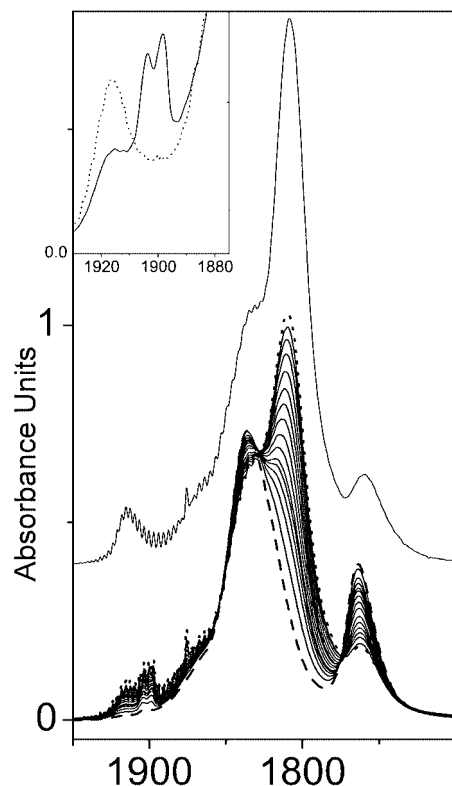
FIG. 7. IR spectra of NO dosed at room temperature (decreasing P_{NO} from 15 Torr, dotted-line spectrum, to 10^{-3} Torr, dashed-line spectrum) on sample FeS50 activated at 773 K for 1 h. This experiment is to be compared with Fig. 6c, in which the $P_{NO} = 15$ Torr spectrum has been vertically shifted for direct comparison. The inset reports the magnification in the region of $Fe^{3+}(NO)$ complexes of the $P_{NO} = 10^{-2}$ Torr spectrum (solid line) and of the comparable spectrum obtained on the catalyst reduced in H_2 (dotted line).

3.4.3. The effect of NO contact time. Unlike CO and N_2O, a clear evolution of the band intensities of adsorbed NO with contact time is observed (Fig. 8). In particular the absorptions at about 1900 and 1835 cm^{-1} reach their maximum intensity immediately after NO admission and then decline with time. Conversely, the bands at 1916 (weak) and 1810 cm^{-1} (strong) increase with time. Two isosbestic points, at 1904 and 1825 cm^{-1}, indicate that the species responsible for the bands at 1900 and 1835 cm^{-1} are gradually transformed into the ones responsible for the bands at 1916 and 1810 cm^{-1}. The inset of Fig. 8 illustrates the gradual formation of very weak absorption in the 2150–2000 cm^{-1} interval. A similar absorption is obtained also by directly dosing NO_2 on the Fe silicalite samples (not shown). Similar results, obtained on the other samples, are not reported, for brevity.

3.4.4. The effect of activation temperature. Although the effect of increasing the activation temperature has been studied on the whole series of samples, for the sake of brevity we only report the results obtained upon adsorp-

tion of NO on sample FeS50 activated at 773, 973, and 1073 K (Figs. 9a–9c, respectively). The inset shows the corresponding zeolite spectra in the OH stretching region before interaction with NO. The 3630 cm^{-1} band (associated with Si(OH)Fe Brønsted acid sites) (32) gradually decreases with increasing activation temperatures, being virtually absent in the sample activated at 1073 K.

The first effect of the increase in activation temperature is a general increase in integrated band intensities. A second observation regards the preferential intensification of the band at 1835 cm^{-1}. Finally, activation at 1073 K (Fig. 9c) causes the formation of two new bands, at 1875 and 1777 cm^{-1}, which disappear upon decreasing P_{NO}.

3.4.5. The effect of water preadsorption. The IR spectra of NO adsorbed on sample FeS50 activated at 773 K for 1 h, contacted with H_2O, and subsequently evacuated at room temperature are reported in Fig. 10b. By comparing Fig. 10b with Fig. 10a (same experiment before H_2O dosage) we observe that preadsorption of water causes (i) a remarkable narrowing and intensification of the bands at 1916, 1810, and 1765 cm^{-1}, (ii) the disappearance of the doublet around

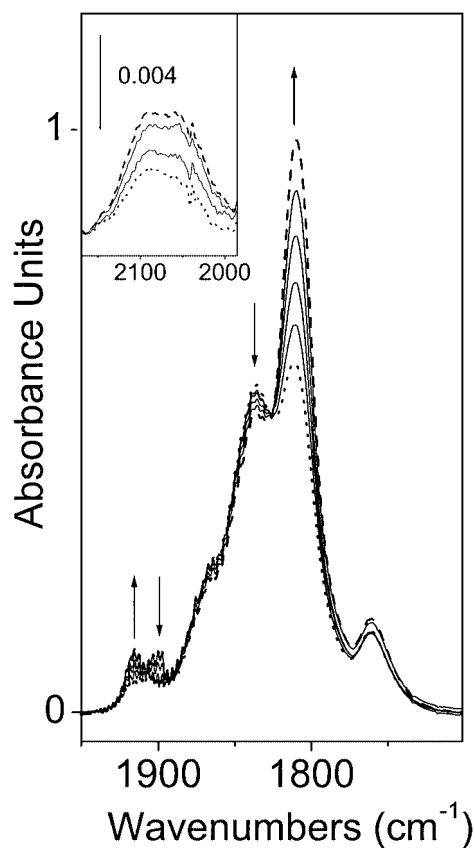**FIG. 8.** Evolution with contact time of the IR spectra of NO adsorbed at room temperature ($P_{NO} = 15$ Torr) on sample FeS50 activated at 773 K for 1 h. Dotted- and dashed-line spectra were registered after a few seconds and 1 h, respectively. The inset reports the evolution of the oxidation products in the 2170- to 1985-cm^{-1} range.

FIG. 9. IR spectra of NO dosed at room temperature (decreasing P_{NO} from 15 Torr, dotted-line spectrum, to 10^{-3} Torr, dashed-line spectrum) on sample FeS50 activated at 773 (a), 973 (b), and 1073 K (c). The inset reports the O–H stretching region of the three experiments before NO adsorption.

1900 cm^{-1}, and (iii) the intensity decrease and narrowing of the band at 1835 cm^{-1}. Similar results, obtained on the other samples, are not reported, for brevity.

3.4.6. The effect of oxidation with O_2 and N_2O. The effect of oxidation (with O_2 or N_2O at different temperatures) was studied on the whole series of samples previously activated at different temperatures. We report only the results obtained on sample FeS50 previously outgassed at 773 K. The oxidation has been performed at room temperature and at 523 K with both O_2 and N_2O. As the room temperature treatment with N_2O does not cause significant changes
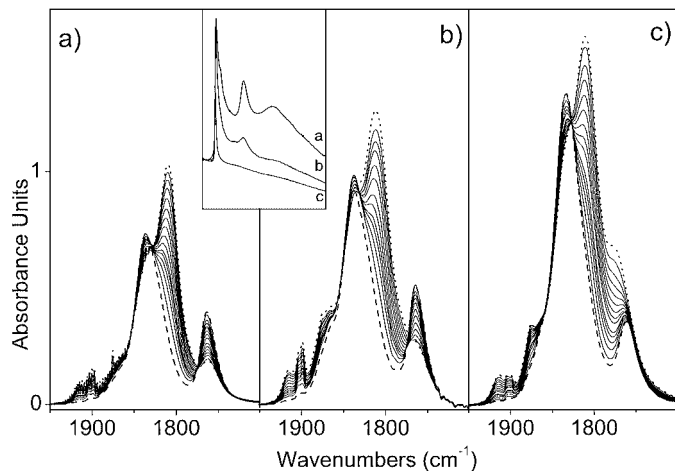

FIG. 10. IR spectra of NO dosed at room temperature (RT) (decreasing P_{NO} from 15 Torr, dotted-line spectrum, to 10^{-3} Torr, dashed-line spectrum) on sample FeS50 activated at 773 K (a) and after subsequent H_2O dosage at RT and RT reevacuation (b).
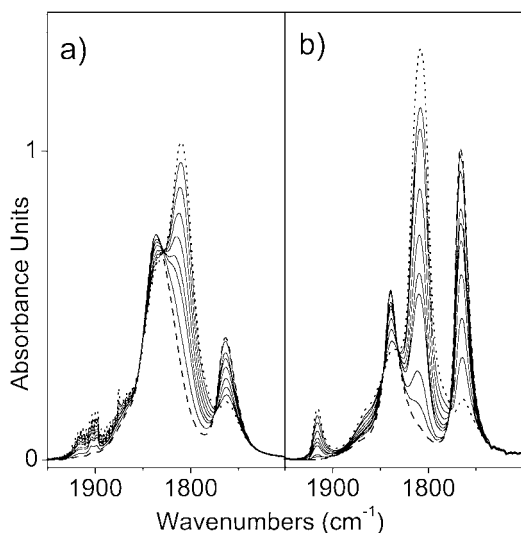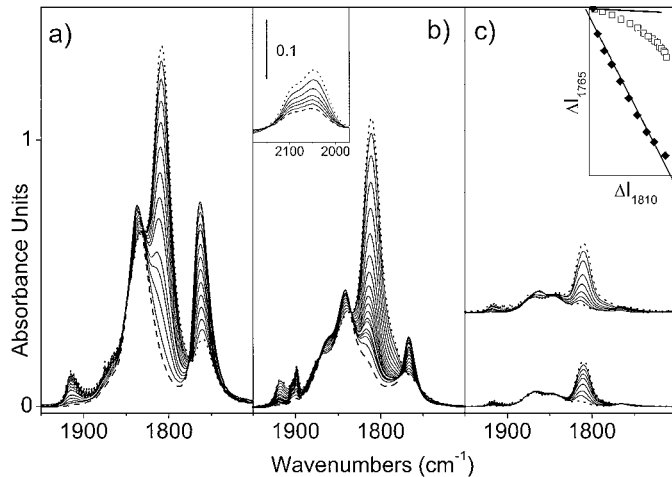

FIG. 11. IR spectra of NO dosed at room temperature (RT) (decreasing P_{NO} from 15 Torr, dotted-line spectrum, to 10^{-3} Torr, dashed-line spectrum) on sample FeS50 activated at 773 K (a) and after subsequent oxidation with O_2 at RT (b) and at 523 K (c, lower spectra). (c) The same experiment obtained after oxidation with N_2O at 523 K vertically shifted. (b) Inset shows the evolution of the spectra in the 2170- to 1985-cm^{-1} range, where oxidation products are observed. (c) Inset shows ΔI_{1765} vs ΔI_{1810} (see caption of Fig. 6) for all experiments shown in Fig. 11 (part a, ◆; part b, □; part c, solid line).

in the spectra of adsorbed NO, the corresponding spectra are not reported.

For comparison Fig. 11a reports the spectra obtained before oxidation. After interaction with O_2 at room temperature we notice (Fig. 11b) the increase in 1900 cm^{-1} absorption and the parallel decrease in the bands at 1916, 1835, 1810, and 1765 cm^{-1}. Among these, the bands at 1916 and 1810 cm^{-1} are less affected. In the inset of Fig. 11b we illustrate the formation of a very weak absorption in the 2150- to 2000-cm^{-1} range. The same absorption is obtained also by directly dosing NO_2 on the Fe silicalite samples (not shown).

The effect of interaction with O_2 and N_2O at 523 K is reported in Fig. 11c. The effect of oxidation is similar for both reagents: we observe a remarkable inhibition of the capacity of Fe species to adsorb NO, the overall intensity of the NO bands being reduced by a factor of ca. 8. Furthermore, we do not observe the usual correlation between the band at 1810 and the one at 1765 cm^{-1}. This is illustrated in the inset of Fig. 11c, where the plots of ΔI_{1765} vs ΔI_{1810} are reported for the sample before oxidation (◆) and after oxidation at room temperature (open square) and at 523 K (full line). In the latter case, because of the low intensity of the NO spectra, the plot of the experimental ΔI_{1765} and ΔI_{1810} would result in a concentration of all points in the left upper corner of the inset. Therefore we have reported the linear extrapolation of such data. Also in this case IR bands were observed in the 2150- to 2000-cm^{-1} range (not shown).

3.4.7. The effect of reduction with H_2 at increasing temperatures.

The effect of reductive treatments with H_2 has been investigated on the whole series of samples. For the sake of brevity we report the results obtained on sample FeS150 previously outgassed at 973 K (Fig. 12a for comparison) and subsequently reduced at 573 (Fig. 12b) and 873 K (Fig. 12c). From these data it is inferred that reduction with H_2 causes an increase in overall band intensities, a phenomenon more evident for the sample reduced at the highest temperature (Fig. 12c). It is worth noticing that the 1900 cm^{-1} band is never observed on reduced samples.
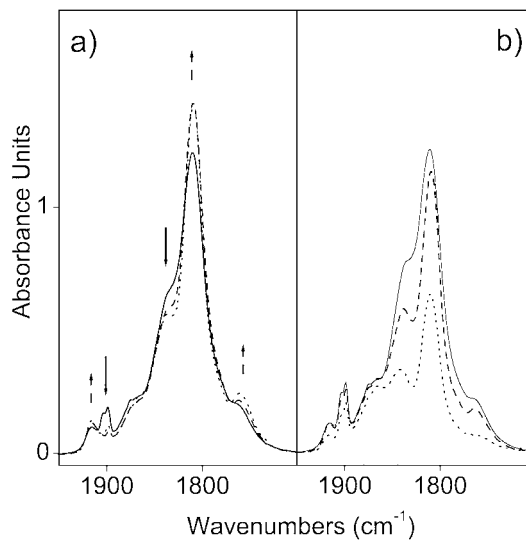
3.4.8. The effect of heating in NO.

A further set of IR experiments reports the IR spectra of NO on the FeS50 catalyst previously contacted with NO at 373, 473, 573, and 673 K and then cooled at room temperature. The data can be divided into two parts. For $T \leq 473$ K (Fig. 13a) we observe a decrease in two components, at 1900 and 1835 cm^{-1} (full arrows), and an increase in the bands at 1916, 1810, and 1765 cm^{-1} (broken arrows). A similar trend was observed when the contact time at room temperature was increased (Section 3.4.3). For $T \geq 573$ K (Fig. 13b), the situation is different, as all bands, at 1916, 1835, 1810, and 1765 cm^{-1}, are gradually reduced. Simultaneously, a small increase in the doublet at 1900 cm^{-1} is observed. This effect is similar to what was found in the experiments illustrating the effect of oxidation (Section 3.4.6).

3.5. EPR Spectra of Fe Silicalite before and after NO Contact

Figure 14 reports the spectral profile of the FeS90 sample after different treatments. The spectrum at the top (outgassed at room temperature) is characterized by two groups
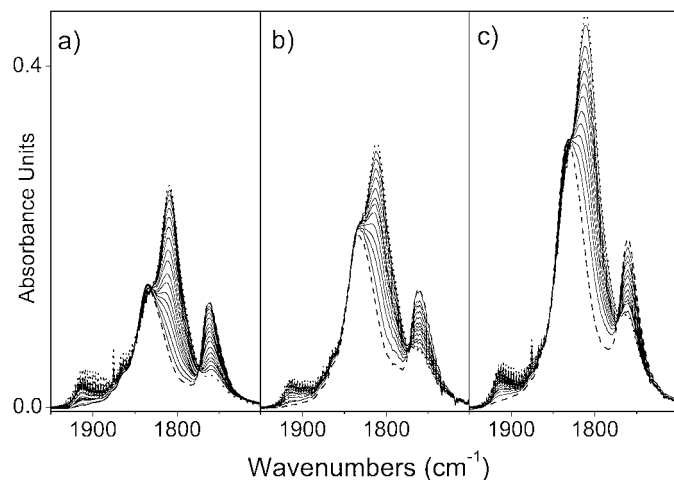
FIG. 13. IR spectra of NO dosed at room temperature ($P_{NO} = 15$ Torr, solid line in both parts a and b) on FeS50 activated at 773 K. (a) The $P_{NO} = 15$ Torr for 373 and 473 K (dashed and dotted lines, respectively). (b) As in part a for 573 and 673 K (dashed and dotted lines, respectively).

of signals. The first group is constituted by a line at $g' = 4.3$ and by some other lines at higher g'. The second group is a single broad line centered at about $g = 2$. Progressive outgassing up to 773 K (associated with dehydration of the solid[2]) has two basic effects on the EPR spectra (see Figs. 14a–14c). The first effect is the disappearance of the broad band at $g = 2$, which looses its intensity upon dehydration. The phenomenon is reversible and the band reappears upon rehydration (see Fig. 14e) of the catalyst. The second effect is an increase in the definition of the low-field part of the spectra. Along with dehydration the EPR spectra decrease in intensity. This decrement becomes relevant on the samples activated at 773 K (Fig. 14c) and at 973 K (not shown). After activation at 973 K, the low-field-structured portion of the spectrum ($g' = 4.3$) is nearly completely eroded and is replaced by a broad unstructured signal. Oxidation with N_2O (after activation at 773 K) results in recovery of the initial intensity although with a slightly different profile (cf. Figs. 14d and 14a). Subsequent interaction with water results in spectrum (Fig. 14e), whose intensity reaches about twice that of the starting signal (Fig. 14a).

The interaction of NO with sample FeS90 dehydrated at 773 and 973 K brings about the formation of various signals in the central region of the EPR spectrum (g around 2) which are destroyed after removing nitric oxide from the

FIG. 12. IR spectra of NO dosed at room temperature (decreasing P_{NO} from 15 Torr, dotted-line spectrum, to 10^{-3} Torr, dashed-line spectrum) on sample FeS150 activated at 973 K (a) and after subsequent reduction with H_2 at 573 (b) and 873 K (c).

[2] Since water is a strong IR absorber, IR spectra are unable to follow the first stages of the activation procedure. This problem is not present in EPR spectroscopy; therefore we report data concerning the activation at 273 and 573 K, which mainly concerns the elimination of physisorbed water.
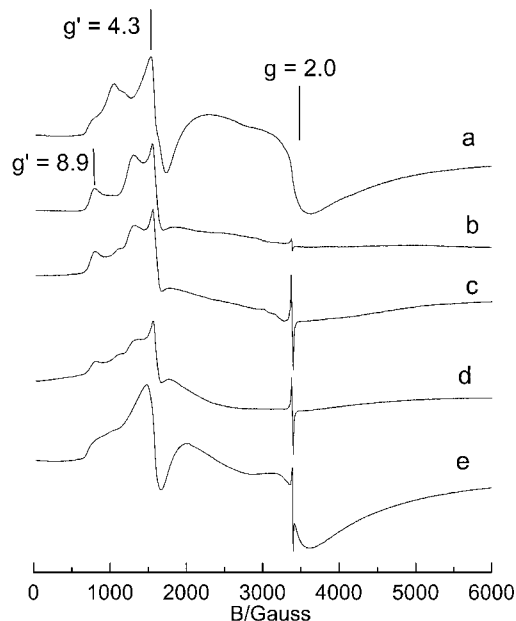
FIG. 14. EPR spectra of FeS90 catalyst at 77 K after activation at room temperature (a), at 573 (b), and at 773 K (c); *in situ* oxidation with N_2O at 523 K (d) and rehydration at room temperature (e).

FIG. 15. From top to bottom: EPR spectra of FeS90 catalyst activated at 773 K and measured at 77 K, after *in situ* contact with NO at room temperature ($P_{NO} = 15$ Torr), and subsequently evacuated at room temperature. (Inset) The last two spectra magnified in the 3100- to 3600-G range.
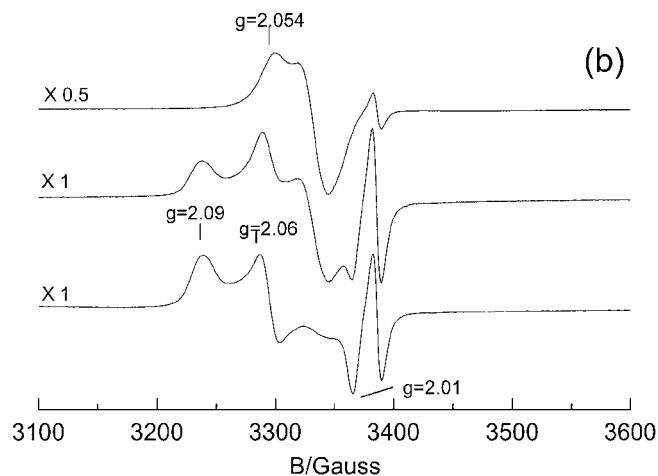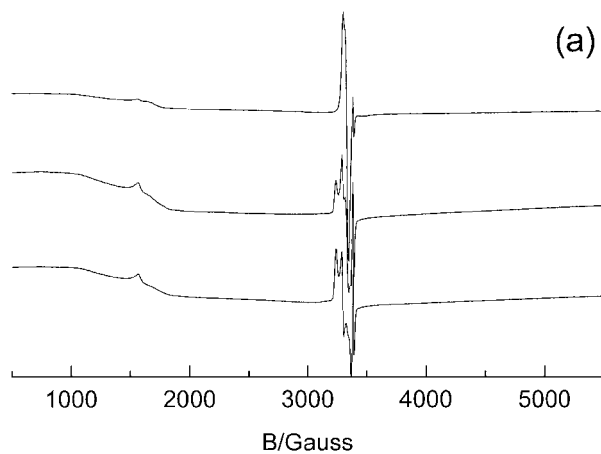

FIG. 16. EPR spectra of NO dosed on FeS90 catalyst previously activated at 973 K and measured at 77 K. From top to bottom, effect of decreasing P_{NO} from 15 to 10^{-3} Torr. (a) Whole X-band range; (b) zoom in the 3100- to 3600-G range.

surface. For both activation temperatures, the spectra observed after adsorption of NO are similar but not equal. In the case of dehydration at 773 K (Fig. 15) the intensity of the nitrosyls is rather low and its spectral profile broad and ill defined, while in the case of activation at 973 K they have more intense and better-resolved signals (Fig. 16b).

First of all, there is a marked dependence of the spectral profile upon P_{NO}. Figure 16b shows that under $P_{NO} = 15$ Torr (first spectrum from top) the signal is nearly axial ($g_{\parallel} = 2.054 > g_{\perp} = 2.02$), whereas after a brief outgassing at room temperature a rhombic signal appears in the same spectral region (bottom spectrum), with three distinct values of the diagonal terms of the g tensor ($g_1 = 2.09$, $g_2 = 2.06$, $g_3 = 2.01$). For an intermediate situation ($P_{NO} \approx 3$ Torr) the features of both described signals are present in the spectrum (second from top), thus illustrating the pressure dependence of the Fe^{2+}/NO interaction.

4. DISCUSSION

4.1. EXAFS Spectroscopy and the Heterogeneity of Extraframework Iron Species

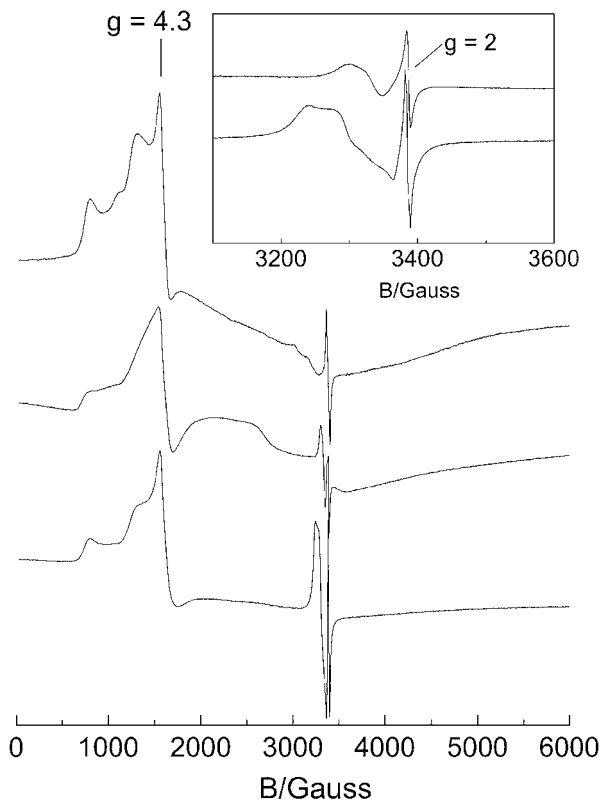The dramatic reduction in the EXAFS signal after activation (Fig. 1a) cannot be explained only in terms of an extremely high coordinative unsaturation. In fact, when Fe atoms occupy tetrahedral framework positions, they have a well-defined and ordered first-shell environment. This situation gives rise to a constructive integration of the EXAFS signals, yielding (within experimental errors) a Fe–O coordination number of 4. However, when a fraction of iron atoms migrates, forming more than one extraframework species, the local environment of the Fe atoms has a consistent spread in Fe–O bond distances, dynamic Debye–Waller factors, and coordination numbers. As a consequence, such an EXAFS signal is affected by a large Debye–Waller factor (of static origin), which causes the intensity reduction (33). As a consequence, a quantitative EXAFS data analysis is meaningful only before template removal. For the activated samples EXAFS indicates only the high heterogeneity of iron species.

The absence of any significant higher shell contributions means that we cannot detect the presence of dimeric species observed by some authors (9, 12) on Fe-exchanged zeolites characterized by a higher iron concentration. We conclude that either dimeric species are formed only at higher Fe content or that their contribution in a Si/Fe = 90 sample is below the detection capability of the technique. The same holds for clustered species of small dimension. Conversely, large three-dimensional aggregates of Fe_2O_3 should give a detectable signal. As no such signal is observed, they are ruled out on sample FeS90 activated *in vacuo* at 773 and 973 K.

4.2. High-Resolution XANES Spectroscopy: The Oxidation State of Iron

XANES spectroscopy is one of the most informative techniques in the determination of oxidation states and of local symmetry of transition metal ions (34). This is particularly true when appropriate model compounds, with well-defined oxidation and coordination states, are available for comparison (9, 12). Among the compounds used in this work, $FePO_4$ is a nearly perfect model for Fe in tetrahedral coordination, having two O at 1.82 Å and two at 1.87 Å (35). As far as the octahedral Fe^{3+} models are concerned, $Fe(acac)_3$ is characterized by a quite perfect octahedral geometry (36) (six Fe–O distances in the range 1.97–2.02 Å), while the Fe^{3+} ions in α-Fe_2O_3 have a distorted symmetry, with three Fe–O distances at 2.11 Å and three at 1.94 Å (37). Crystalline ferrocene has a molecular center of symmetry, i.e., a staggered configuration of D_{5d} symmetry.

The XANES spectra of the model compounds (Fig. 2a) show that the K-edge position is mainly dependent upon the oxidation state of the atom. In fact, the three ferric compounds exhibit the K-edge at higher energy (7122.5–7123.4 eV) than does $FeCp_2$ (7119.4 eV). The smallest difference between the three ferric compounds, less than 1.0 eV, is determined by the coordination ligands and their local symmetry around the absorbing atom. A similar correlation with the oxidation state is found for the $1s \rightarrow 3d$ preedge peak position: while the three ferric compounds show signals around 7114 eV, the peak of $FeCp_2$ is at lower energy (7112.5 eV). Furthermore, while $FePO_4$ gives a relatively intense signal at 7114 eV, two components of much lower intensity are observed for Fe^{3+} in octahedral symmetry. The difference in intensity can be explained in terms of local symmetry around the absorbing atom. In fact, the $A_{1g} \rightarrow T_{2g}$ and $A_{1g} \rightarrow E_g$ transitions are symmetry forbidden (Laporte law) for Fe^{3+} in octahedral coordination, while the $A_1 \rightarrow T_2$ transition is allowed in tetrahedral Fe^{3+}. The higher intensity observed for Fe_2O_3 reflects a higher distortion from the ideal octahedral symmetry with respect to $Fe(acac)_3$.

Figure 2b reports the spectra of FeS90 containing the template and after thermal treatments at increasing temperatures. Before template burning, the intensity of the $1s \rightarrow 3d$ preedge peak is even higher than that of $FePO_4$ (0.205 vs 0.133), indicating that the local symmetry of Fe^{3+} is closer to the ideal tetrahedral one than in $FePO_4$. The edge position is evidently shifted from 7123.6 eV for the sample measured with the template to 7122.4 and 7120.6 eV for the samples activated at 773 and 973 K, respectively. These data suggest that, after the thermal activation, framework Fe^{3+} species undergo a progressive reduction to Fe^{2+}. The thermal treatment causes a reduction of the $1s \rightarrow 3d$ peak intensity (inset of Fig. 2b), demonstrating the evident migration of iron species from framework tetrahedral positions. Simultaneously, a low-energy shoulder appears around 7111.8 eV, whose intensity increases with an increase in activation temperature. Its energy position is close to that observed for $FeCp_2$ (7112.5 eV). However, a higher full width indicates the presence of more than one Fe^{2+} species. These results indicate that a significant fraction of iron in the activated sample is in the divalent state.

Upon oxidation with N_2O on the sample activated at 973 K (Fig. 2c) the edge position shifts back from 7120.6 to 7123.1 eV, indicating a nearly complete restoration of Fe^{3+} species. The same conclusion can be reached by observing the total erosion of the 7111.8 eV component of the $1s \rightarrow 3d$ preedge peak (Fig. 2c, inset). A similar trend was observed with the sample activated at 773 K.

Figure 3 reports the effect of oxidation on the FT of the EXAFS spectra. Unfortunately, due to the heterogeneity of the iron species present in the sample, a reasonable fit of the EXAFS spectrum cannot be done. Nevertheless, the macroscopic variation of the first shell signal indicates that a considerable fraction of iron ions has undergone an important modification of its coordination sphere, with the addition

of an oxygen ligand at a rather short Fe–O distance. Of course, this could be the adsorbed oxygen atom produced upon N_2O decomposition, indicated by Sobolev *et al.* to be the active species in partial oxidation reactions (16).

4.3. Assignment of the IR Spectra of CO and N_2O Adsorbed on Activated, Oxidized, and Reduced Samples: Relation with the Oxidative State of Iron

The CO spectra of Fig. 4a can be described as follows. The peak at 2138 cm^{-1} is due to physically adsorbed CO (32, 38). The composite absorption centered at 2173 cm^{-1} (with a shoulder at ~2162 cm^{-1}) and the weaker absorption at 2215 cm^{-1} are due to CO adsorbed on extraframework or partially extraframework Fe^{x+} ($x = 2$ or 3) species. In fact Fe^{3+} in framework positions is fully inactive (32). Furthermore, the nearly total absence of the band at 3630 cm^{-1} associated with the framework Si(OH)Fe groups (Fig. 4, inset) indicates that nearly all iron is in extraframework positions.

By analogy with the results obtained on zeolites containing extraframework Al^{3+} (38), we assign the weak peak at 2215 cm^{-1} to CO adsorbed on extraframework Fe^{3+} species characterized by a strong local electrical field. IR spectra of CO adsorbed on α-Fe_2O_3 (39), where surface Fe^{3+} ions are fivefold coordinated and associated with weaker fields, show C–O bands in the 2175- to 2155-cm^{-1} region. This suggests that the structured 2173- to 2162-cm^{-1} band is partially due to CO adsorbed on highly shielded ferric ions. However, the $Fe^{3+}\cdots CO$ adducts on α-Fe_2O_3 easily decompose upon decreasing P_{CO}, which is not the case for the bands observed in Fig. 4a. A different type of CO adducts must consequently be invoked. We tentatively ascribe the strongly bonded fraction of the band 2173–2162 cm^{-1} to $Fe^{2+}\cdots CO$ adducts in which, besides electrostatic effects, overlap forces are present. Notice that the intensity of the 2215-cm^{-1} band is at least one order of magnitude smaller than the 2173- to 2162-cm^{-1} absorption. This means that the concentration of extraframework Fe^{3+} species in the sample activated at 973 K is smaller than that of the Fe^{2+} species. Similar results (not adding further information) were obtained on samples activated at 773 K. This is in agreement with XANES data.

Further information comes from CO adsorption on the oxidized sample (Fig. 4b). After oxidation the bands attributed to $Fe^{x+}\cdots CO$ adducts ($x = 2$ or 3) are severely weakened. In this case it is possible to observe the peak at 2155 cm^{-1} due to CO hydrogen bonded to the external silanols. This band, the only one observed upon CO adsorption on silicalite (40), was totally obscured by the $Fe^{2+}\cdots CO$ adducts manifestation shown in Fig. 4a. The absence of $Fe^{x+}\cdots CO$ adducts on the oxidized sample indicates that the coordinative vacancies of extraframework Fe^{2+} and Fe^{3+} ions were filled with oxygen. Similar results were obtained on samples oxidized with N_2O and agree

with the XANES and EXAFS results (Section 4.2). We conclude that extraframework Fe^{2+} ions can be oxidized by O_2 and N_2O at 523 K. It is thus confirmed that N_2O decomposes on iron centers with formation of adsorbed oxygen, as proposed by Sobolev *et al.* (16). However, from these results the structure of adsorbed oxygen cannot be inferred.

The effect of reduction in H_2 can be appreciated by comparing Figs. 4a and 4c. The only relevant difference is the nearly total erosion of the 2215-cm^{-1} band. This is in agreement with the assignment to linear $Fe^{3+}\cdots CO$ adducts. Conversely, the 2173- to 2156-cm^{-1} adsorption remains unaltered, confirming its attribution to CO adducts on reduced Fe^{2+} species.

Note that all $Fe^{x+}\cdots CO$ adducts have a monocarbonyl character and are formed through an apparently nonactivated process. This indicates that the CO adsorption process can be described as an addition reaction into the vacant coordination sphere of Fe, following the path

$$Fe^{3+} \xrightarrow{CO} Fe^{3+}\cdots CO, \qquad [1a]$$

$$Fe^{2+} \xrightarrow{CO} Fe^{2+}\cdots CO. \qquad [1b]$$

The relatively weak interaction between CO and iron ions makes this ligand only able to discriminate between Fe species in different oxidation states, without discriminating between different coordination states. Hence a detailed and systematic discussion of CO spectra on all Fe silicalite samples does not add further information.

The adsorption of N_2O (Fig. 5) generates three bands, at 2275, 2235, and 2218 cm^{-1}. The first two are attributed to N_2O adsorbed on Fe^{3+} and Fe^{2+} centers, respectively. The strong and narrow band at 2218 cm^{-1} (with a shoulder at 2200 cm^{-1}) is due to physically adsorbed N_2O and is the only one present on silicalite (dotted line in Fig. 5). The frequencies of N_2O adsorbed on Fe^{3+} (a) and Fe^{2+} (b) and physically adsorbed (c) are on the order of $\nu_a > \nu_b > \nu_c$. This demonstrates that the interactions involved are mainly of an electrostatic nature, as found for CO. Similarly to what was observed with CO, upon oxidation with O_2 or N_2O at 523 K, the 2275 and 2235 cm^{-1} bands are severely weakened (not shown).

Finally, the peak of N_2O adsorbed on Fe^{3+} sites is stronger than expected on the basis of the results obtained with CO. This can be explained in terms of differences in the extinction coefficients of the involved bands.

4.4. IR Spectra of Adsorbed NO and Their Relation with the Oxidation, Coordination, and Clustering State of Adsorbing Sites

4.4.1. The effect of Fe concentration. The overall intensity of the IR spectra in the NO stretching region increases with an increase in Fe concentration (Figs. 6a–6d).

TABLE 2

Assignment of the Nitrosyl Bands to Iron Complexes

Complexes	Frequencies
$L_2N_3Fe^{2+}(NO)$	1835 cm^{-1}
$L_2N_2Fe^{2+}(NO)_2$	$1835 \text{ and } 1765 \text{ cm}^{-1}$
$L_2NFe^{2+}(NO)_3$	$1916 \text{ and } 1810 \text{ cm}^{-1}$
$L_3M_mFe^{3+}(NO)$	1900 cm^{-1}

Note. A difference of $\pm 3 \text{ cm}^{-1}$ can be observed upon different activation procedures, iron content, and NO coverage.

However, this increase is not linear. This reflects a progressive reduction of the fraction of coordinatively unsaturated surface iron species with a lowering of the Si/Fe ratio and suggests the formation of inactive oxidic clusters at the highest iron content.

Spectra showing similar N–O stretching bands were reported by several authors (18, 22–26) for Fe-loaded siliceous materials after reduction with H_2 or CO. In analogy with homogeneous $Fe^{2+}(NO)_n$ complexes all authors agree that they have to be attributed to nitrosyl complexes formed on Fe^{2+} sites.
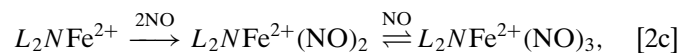
All spectra essentially consist of four main bands coupled in two pairs (Table 2). The first pair (1916, 1810 cm^{-1}) decreases simultaneously with P_{NO}, while the second pair (1835, 1765 cm^{-1}) behaves in the opposite way. The intensity decrease of the 1810 cm^{-1} band (ΔI_{1810}) correlates linearly with ΔI_{1916}, indicating that we are dealing with two IR features of the same nitrosyl species (inset, Fig. 6a). A similar quantitative correlation is not possible for the 1835/1765-cm^{-1} pair, because a fifth component contributes to the 1835-cm^{-1} band (*vide infra*). However, previous IR experiments with an isotopic $^{14}NO/^{15}NO$ mixture (18) have demonstrated that the 1835/1765-cm^{-1} bands are due to the symmetric and asymmetric stretching modes of a $Fe^{2+}(NO)_2$ complex. These complexes are reversibly transformed by addition of a NO ligand. This is indicated by the presence of two isosbestic points, at 1830 and 1775 cm^{-1}. Moreover, the ΔI_{1810} correlates linearly with the increase in the band at 1765 cm^{-1} upon P_{NO} reduction (inset Fig. 6b). The 1916/1810-cm^{-1} doublet is thus ascribed to a $Fe^{2+}(NO)_3$ complex (symmetric and asymmetric ν(N–O), respectively), as confirmed by isotopic substitution experiments (18).

The $Fe^{2+}(NO)_2 \leftrightarrow Fe^{2+}(NO)_3$ equilibrium holds for the majority of the dinitrosyl complexes but not for all. In fact, particularly on the Fe-richest samples, the band at 1765 cm^{-1} does not disappear, even at the highest P_{NO}. This suggests that the extraframework Fe^{2+} species are heterogeneous. This heterogeneity can be appreciated also in the inset of Fig. 6b, where the deviation from the ideal linear behavior is higher than that observed in the plot of ΔI_{1810} vs ΔI_{1916}. In fact, the latter data concern the sites forming

the trinitrosyl adducts only, while the former contain the whole set of $Fe^{2+}(NO)_2$ complexes.

Underneath the high-frequency component of the dinitrosyl species (1835 cm^{-1}) a broad band is observable in the 1850- to 1820-cm^{-1} range, whose relative intensity grows with the Fe concentration. This band, which is scarcely affected by P_{NO}, is assigned to mononitrosyl groups prevalently adsorbed on a third family of Fe^{2+} sites. In the following we argue in favor of the hypothesis that these species are present in dimeric or larger clusters.

All results reported in Fig. 6, although rather complex, can be explained using the simple assumption that we are dealing with $L_2N_nFe^{2+}$ centers, where L is a framework SiO^- (or atomic O^{2-}) chemically linked group and N is a framework oxygen atom of the vicinal SiOSi bridges electrostatically linked. The value of n depends upon the location of the ions on the framework walls and defects. When probed with NO, the $L_2N_nFe^{2+}$ species are shown to be a composite family of sites, able to add either only one, two, or three NO ligands, i.e., L_2NFe^{2+}, $L_2N_2 Fe^{2+}$, and $L_2N_3 Fe^{2+}$. On this basis, the formation of the mono-, di-, and trinitrosyl species can be described as

$$L_2N_3Fe^{2+} \xrightarrow{\text{NO}} L_2N_3Fe^{2+}(NO), \qquad [2a]$$

$$L_2N_2Fe^{2+} \xrightarrow{\text{2NO}} L_2N_2Fe^{2+}(NO)_2, \qquad [2b]$$

$$L_2NFe^{2+} \xrightarrow{\text{2NO}} L_2NFe^{2+}(NO)_2 \rightleftharpoons L_2NFe^{2+}(NO)_3, \quad [2c]$$

where the addition of NO occurs on structurally different sites and where the number of adsorbed NO is greater on the most coordinatively unsaturated sites.

When probed with CO and N_2O, Fe^{2+} species behave as a unique family of sites able to add a single ligand to their incomplete coordination sphere via electrostatic interactions. Conversely, when probed with NO (due to the presence of $d-\pi$ overlap forces), structural information can be obtained on the Fe^{2+} local structure. The considerably higher stability of dinitrosyl species, with respect to the monocarbonylic ones, reflects the situation already observed for Cr^{2+}/SiO_2 (41). As was the case for CO, the main spectroscopic features reported in Fig. 6 concern ferrous species.

4.4.2. The effect of activation time. After short activation procedures, the IR spectra of adsorbed NO show a weaker intensity of the peaks associated with di- and trinitrosyl species and by the presence of a new doublet centered around 1900 cm^{-1} (see full line in the inset of Fig. 7). In agreement with literature data (42), the new doublet is readily assigned to NO adsorbed on two different Fe^{3+} centers. In fact, a NO stretching frequency higher than that of NO gas (1876 cm^{-1}) suggests that NO is adsorbed on Fe sites with lower back-bonding ability (as expected for Fe^{3+}). Furthermore, the peaks at ~1900 cm^{-1} are absent on

samples prereduced in hydrogen (dotted line in the same inset). These considerations, together with the lower intensity of the peaks associated with the di- and trinitrosyl species (Table 2), suggest that the Fe^{3+} extraframework sites can be reduced by prolonged activation treatments (see also XANES) with formation of the $L_2N_nFe^{2+}$ species discussed in the previous paragraph. In conclusion, on samples containing a small iron loading, a mixture of coordinatively unsaturated Fe^{2+} and Fe^{3+} sites is present, whose relative proportion is not easily controlled by the activation conditions. The resulting spectra always lie between those reported in Figs. 6 and 7.

4.4.3. The effect of NO contact time.

The transformation of the IR bands of adsorbed NO with contact time (Fig. 8) can be explained as follows. The absorptions at about 1900 and 1835 cm^{-1}, assigned to $Fe^{3+}(NO)$ and $Fe^{2+}(NO)$ complexes, respectively, reach their maximum intensity immediately after NO admission and then decline with time. These bands are thus associated with a nonactivated adsorption process similar to that found for CO and N_2O. Notice that at 1835 cm^{-1} also the $\nu_{sym}(N–O)$ of the $Fe^{2+}(NO)_2$ complexes occurs (Table 2). However, the invariance of the band at 1765 cm^{-1}, due to the $\nu_{asym}(N–O)$ of the $Fe^{2+}(NO)_2$ complexes, indicates that only the $L_2N_3Fe^{2+}(NO)$ complexes decrease with contact time.

The decrement of the 1900-cm^{-1} doublet with contact time is readily interpreted in terms of a reduction process, whereby the Fe^{3+} species are reduced to Fe^{2+} species. The formation of the related oxidation products is documented by the absorption in the interval 2150–2000 cm^{-1} whose intensity increases with time (see inset of Fig. 8). The same absorption is obtained also by directly dosing NO_2 on the Fe silicalite samples (not shown). As this process is associated with the increase in the bands at 1916 and 1810 cm^{-1}, we can conclude that ferric sites, giving rise to $Fe^{3+}(NO)$ complexes, are reduced to ferrous sites able to absorb up to three NO molecules, i.e., L_2NFe^{2+} species.

This reduction path does not explain the simultaneous decrease of $Fe^{2+}(NO)$ complexes. A plausible explanation of the observed data is in terms of a NO-promoted ligand displacement (43). In other words, the formation of polynitrosyl complexes on Fe^{2+} species is (at least for a fraction of sites) an activated process. We infer that, in the presence of a high equilibrium pressure, a small fraction of the Fe^{2+} sites progressively lose the weakly bonded N ligands in favor of NO molecules, following the path $L_2N_3Fe^{2+}(NO) \rightarrow L_2N_2Fe^{2+}(NO)_2 \rightarrow L_2NFe^{2+}(NO)_3$. This hypothesis was validated by performing the same experiment on a FeS50 sample previously reduced in H_2. In this case, as $Fe^{3+}(NO)$ complexes are totally absent, the increase in the trinitrosyl bands can be ascribed in a straightforward manner to the decrease in the $Fe^{2+}(NO)$ band at 1835 cm^{-1} only (not shown).

To confirm that the activated process involves only a fraction of the Fe^{2+} species, we adsorbed NO on a FeS50 sample at 77 K. The NO spectra (not shown) show the simultaneous presence of bands of both $Fe^{2+}(NO)_2$ and $Fe^{2+}(NO)_3$ complexes also at low temperature. This demonstrates that the majority of $Fe^{2+}(NO)_3$ species are formed through a nonactivated process.

4.4.4. The effect of activation temperature.

The gradual decrease in the 3630-cm^{-1} band, associated with Si(OH)Fe Brønsted acid sites, by increasing the activation temperature (see inset of Fig. 9) reflects the migration of iron into extraframework positions (32). Besides this, a broader absorption (centered at 3500 cm^{-1}) is observed in the spectrum of sample FeS50 activated at 773 K (Fig. 9 spectrum a). This band is due to H-bonded OH groups in internal defective cavities, often labeled hydroxylated nests (2, 44). Activation at 973 K causes the nearly total disappearance of this spectroscopic feature, indicating that internal OH groups were eliminated with the formation of new strained Si–O–Si bridges.

The overall intensity of NO adducts increases upon increasing the activation temperature. However, as observed during the discussion of the effect of iron loading (Section 4.4.1), the integrated intensity of the nitrosyl bands does not increase proportionally to the concentration of extraframework iron species. This is particularly evident if we compare the relatively small increase in the NO bands (Figs. 9a vs 9c) with the dramatic erosion of the Si(OH)Fe band (totally absent in the sample activated at 1073 K). This indicates that a fraction of extraframework iron species are not accessible to NO, probably because of three-dimensional clustering processes. X-ray diffraction (XRD) analysis shows the high crystalline quality of FeS50 even after activation at 1073 K, without revealing the presence of any other phases.

The formation of new bands at 1875 and 1777 cm^{-1} on the sample activated at 1073 K indicates the formation of new extraframework iron species. Similar IR spectra were obtained on mesoporous Fe–MCM–41 samples, where iron is supposed to be grafted to an amorphous siliceous matrix (not shown). The band at 1835 cm^{-1} (assigned to $L_2N_3Fe^{2+}(NO)$ complexes) increases with an increase in activation temperature. As the activation at high temperature increases the number of extraframework species, and hence favors clustering, we suggest that the $L_2N_3Fe^{2+}$ species are not isolated.

4.4.5. The effect of water preadsorption.

IR spectra of NO adsorbed on FeS50, previously contacted with H_2O and subsequently evacuated at room temperature (Fig. 10b), show a remarkable narrowing and intensification of the bands assigned to $L_2NFe^{2+}(NO)_3$ species (bands at 1916 and 1810 cm^{-1}). Moreover, an important difference is the virtually total absence of the $Fe^{3+}(NO)$ complexes absorbing at around 1900 cm^{-1}. This means that Fe^{3+} species

form stable $Fe^{3+}(H_2O)_n$ complexes upon water contact and water is not displaced by NO.

The promoting effect of H_2O on the formation of trinitrosyl species could be due to a ligand displacement reaction (43), where H_2O extracts the Fe^{2+} ions from the original coordination sphere, favoring the multiple addition of NO ligands. Thus, in the case of ferrous sites, NO is able to displace H_2O ligands, thanks to its high affinity for ferrous species. Notice that, after water adsorption, we can obtain the correct intensity ratio $I_{\nu asym}/I_{\nu sym}$ expected for a dinitrosyl complex (41). A ligand displacement effect is obtained also by adsorbing water on preformed $Fe^{3+}(NO)$ and on $L_2N_3Fe^{2+}(NO)$ complexes, as proved by time-resolved experiments (not shown). In this case $Fe^{3+}(NO)$ and $L_2N_3Fe^{2+}(NO)$ complexes disappear while the di- and trinitrosyl do not.

4.4.6. The effect of oxidation with O_2 and N_2O. After interaction with O_2 at room temperature (cf. Figs. 11a and 11b) an increase in the 1900-cm^{-1} components ascribed to $Fe^{3+}(NO)$ adducts is observed, while ferrous nitrosyl complexes are depressed. Among them, $Fe^{2+}(NO)_3$ (bands at 1916 and 1810 cm^{-1}) are sensitively less affected than $Fe^{2+}(NO)$ complexes (1835 cm^{-1}). This means that the ferrous species characterized by the lowest coordinative unsaturation are more reactive toward interaction with O_2 at room temperature. We infer that $L_2N_3Fe^{2+}$ species are present in dimeric or polymeric species, where dissociation of O_2 occurs, with formation of O^{2-} and $(OO)^{2-}$ species bridging pairs of Fe^{3+} ions. Conversely, room temperature oxidation by O_2 of isolated ferrous sites, L_2NFe^{2+}, does not occur. Notice that the adsorbed oxygen gradually reacts with NO and the products of these oxidation processes are observed in the 2150- to 2000-cm^{-1} range (inset of Fig. 11b). Conversely, N_2O is not efficiently decomposed at room temperature (not shown).

The effect of oxidation with O_2 and N_2O at 523 K is reported in Fig. 11c. Also in this case oxidation products were observed in the 2150- to 2000-cm^{-1} range (not shown). Both reagents cause a strong inhibition of the capacity of Fe species to adsorb NO. Furthermore, the change in trinitrosyl bands upon P_{NO} is not accompanied by the usual $Fe^{2+}(NO)_3 \leftrightarrow Fe^{2+}(NO)_2$ transformation (the band at 1765 cm^{-1} does not grow upon lowering P_{NO}). This was partially present also after oxidation in O_2 at room temperature (Fig. 11b) and has been quantitatively monitored by plotting ΔI_{1765} vs ΔI_{1810} (inset of Fig. 11c). The data extracted from the experiment before oxidation (◆) show a consistent increase in the 1765-cm^{-1} band upon reduction of the 1810-cm^{-1} absorption, reflecting the $Fe^{2+}(NO)_3 \rightarrow Fe^{2+}(NO)_2$ transformation. The linearity of this plot indicates that a constant fraction of $Fe^{2+}(NO)_3$ is transformed into $Fe^{2+}(NO)_2$ at each ΔP_{NO}. The same data plotted for the experiment reported in Fig. 11b (open squares) shows a lower ΔI_{1765}. In particular, in the first stage of the des-

orption process, only a fraction of $Fe^{2+}(NO)_3$ complexes is involved in the formation of dinitrosyl adducts while this fraction slightly increases at lower P_{NO}. The trend of the slopes obtained for the three experiments implies that the fraction of $Fe^{2+}(NO)_3$ giving rise to $Fe^{2+}(NO)_2$ is progressively reduced upon increasing the efficiency of the oxidation process.

The most evident conclusion from these oxidation experiments is that adsorbed oxygen (coming either from O_2 or from N_2O) efficiently shields the Fe centers. This oxygen is not rapidly or completely removed by NO via the reduction process, leading to the formation of NO_x and $Fe^{2+}(NO)_3$ species. It is worth recalling that EXAFS spectroscopy showed the addition of an oxygen ligand in the coordination sphere of iron upon contacting FeS90 with N_2O at 523 K (see Fig. 3). A thermal activation of the oxidized samples is needed to remove all adsorbed oxygen and to restore the NO spectra (not shown). However, these considerations cannot explain why, upon reducing P_{NO}, the $Fe^{2+}(NO)_3$ complexes do not originate the $Fe^{2+}(NO)_2$ species, as is usually observed. This phenomenon can be understood by invoking a ligand competition for the same coordination vacancies of Fe^{2+} between NO and the oxidation products (NO_x) formed in the reduction process.

4.4.7. The effect of reduction with H_2 at increasing temperatures. The reduction with H_2 causes an increase in the overall intensities of NO bands. The phenomenon is more evident for the sample reduced at the highest temperature (Fig. 12c). This set of experiments indicates that, even for a diluted sample (Si/Fe = 150), a consistent fraction of iron is still not sampled by NO and that reduction in H_2 decreases this fraction. A still open question concerns the origin and the structure of the new ferrous sites observed by NO upon reduction in H_2.

4.4.8. The effect of heating in NO. NO was shown to behave as a weak reducing agent at room temperature (Section 4.4.3). The experiments reported in Fig. 13a show that NO acts as a reducing agent also when it is contacted with the sample at $T \leq 473$ K. In this case, we observe to a higher extent the same reductive trend: a decrease in the components at 1900 and 1835 cm^{-1} (full arrows) and an increase in the bands at 1916, 1810, and 1765 cm^{-1} (broken arrows). In this case no formation of oxidation products in the 2150- to 2000-cm^{-1} interval was observed, probably because heating causes their desorption from the surface.

The data obtained at $T \geq 573$ K (Fig. 13b) show that this trend does not continue at higher temperatures: in this case new $Fe^{3+}(NO)$ adducts are formed at the expense of ferrous nitrosyl adducts. This testifies to the amphoteric behavior of NO toward Fe species: NO acts as a reducing agent up to 473 K and as an oxidizing one at higher temperatures (when the $2NO \rightarrow N_2 + O_2$ reaction starts to play a role).

4.5. EPR Spectra of Fe Silicalite before and after NO Contact

EPR reveals the presence of ferric ions and provides general information on their coordination state. EPR spectra of Fe silicalite have been reported in the literature (2, 45, 46). They are markedly determined by mutual interactions between unpaired electrons of the $S = 5/2$ system (high-spin Fe^{3+}) leading to so-called zero-field splitting (ZFS), i.e., the separation between the three Kramers doublet states occurring in the absence of an external magnetic field when the ion is in a noncubic coordination environment. For the X-band EPR spectra of Fe^{3+} ions, this results in the appearance of lines at very low magnetic field characterized by high effective g' values. Actually, the transitions originating from the lines in the g' range between 9 and 4.3 are related to the lowest Kramers doublet in the principal directions.

The two groups of signals observed in Fig. 14a can be assigned as follows. The line at $g' = 4.3$ in the first group is typical of many rather distorted ferric systems. The single broad line centered at about $g = 2$ is typical of solvated ferric ions, as previously shown using water and ammonia as solvating agents (2). In fact this band loses its intensity upon dehydration (Figs. 14a–14c) and reappears upon rehydration (Fig. 14e) of the catalyst. Spectral simulation attempts indicated that the experimental profile of the low-field portion of the spectrum is compatible with the presence of a family of species characterized by a rather high ZFS value (about 0.6 cm^{-1}) with an anisotropic (nonaxial) D tensor (D is the tensor ruling the electron spin–electron spin interactions in $S > 1/2$ spin systems). The increase in the definition of this part of the spectrum upon dehydration (Figs. 14a–14c) is related to water depletion and to some small consequent structural rearrangement. By comparing the IR and EPR results, it is concluded that isolated Fe^{3+} sites, which give, upon NO adsorption, the IR doublet around 1900 cm^{-1} and which are preferentially solvated by water (see Section 4.4.5), are the ferric species contributing to the broad $g = 2$ signal.

The moderate decrease in intensity of the EPR spectra along with the first dehydration step (573 K, Fig. 14b) cannot be interpreted in terms of a reduction in the Fe^{3+} ions (the activation temperature is still too low) but to the loss of coordination of the hydrated species. The resulting species are not EPR observable in the window of magnetic field typical of an X band. The true $Fe^{3+} \rightarrow Fe^{2+}$ reduction occurs on the sample activated at 773 K (Fig. 14, curve c): in this case the EPR signal decreases significantly because of the formation of EPR-silent Fe^{2+} species. A more consistent reduction is observed after activation at 973 K, i.e., after an abundant dislodgment of iron from the framework (see Figs. 2b and 9b for the corresponding XANES and IR experiments, respectively). In this case, a nearly complete erosion of the $g' = 4.3$ signal is observed, which is substi-tuted by a broad unstructured signal. This broad signal can be related to the high heterogeneity of the various oxoiron moieties, formed in extraframework positions.

This picture matches previously reported XANES and IR data. Such techniques have also demonstrated the reversibility of the reduction process by subsequent interaction with oxidizing agents such as O_2 or N_2O. The same results are also obtained with EPR. Oxidation with N_2O on the FeS90 sample, previously activated at 773 K, results in the recovery of the initial intensity although with a slightly different profile (cf. Figs. 14d and 14a). Subsequent interaction with water results in spectrum (Fig. 14e), whose intensity reaches about twice that of the starting signal (Fig. 14a). This is still in agreement with the IR observation that Fe^{3+} extraframework ions are able to efficiently coordinate water molecules (Section 4.4.5). Final reactivation of the sample results in a partial decrease in the signal ascribed to partial dehydration. The role of water is thus fundamental for the detection of EPR spectra of Fe silicalite samples, because it affects the signal intensity, the features in the low-field region, and the appearance of the broad signal around $g = 2$.

The EPR signals formed around $g = 2$ upon interaction with NO (Figs. 15 and 16) are assigned to the paramagnetic $Fe^{2+}(NO)_n$ adducts widely discussed in IR spectroscopy.[3] In fact these signals are destroyed after removing NO. The lower intensity of the EPR signal on the sample activated at 773 K agrees with the lower fraction of ferrous ions, revealed by XANES and IR spectroscopies (Sections 4.2 and 4.4.4).

As described in Section 3.5, a nearly axial signal ($g_{\parallel} = 2.054 > g_{\perp} = 2.02$) is present under $P_{NO} = 15$ Torr (top spectrum in Fig. 16b). A rhombic signal appears in the same spectral region (bottom spectrum), with three distinct values of the diagonal terms of the g tensor ($g_1 = 2.09$, $g_2 = 2.06$, $g_3 = 2.01$) after a brief outgassing. A thorough and unambiguous assignment of the two types of paramagnetic nitrosyls is not possible on the basis of EPR spectroscopy alone, mainly because of the absence of the hyperfine structure of N ligands. Furthermore, the class of iron nitrosyls is extremely wide and involves compounds with very different bonding features (47). Thus, an attempt to identify the species observed in Fig. 16 purely on the basis of similarities with molecular compounds is meaningless. As a consequence, we must limit ourselves to a few important points. The spectral region indicates that the observed paramagnetic entities have $S = 1/2$. Nitrosyl adducts with $S = 3/2$, common in coordination chemistry (48) and also found in zeolitic systems (24, 50), seem to be absent in the present case, since they are characterized by EPR signals at lower field values. Moreover, due to the negative

---

[3] As $g = 2$ is the same field region where solvated Fe^{3+} signals occur, NO dosage was made only after the total elimination of hydrated ferric species.

charge present on NO in $S = 3/2$ complexes, the corresponding ν_{N-O} are expected to occur at a lower frequency with respect to the IR bands reported in Section 3.4. The absence of the hyperfine structure (or at least of a structure with a very low coupling constant, around 1–3 G) is not uncommon in iron nitrosyls (51) and is observed in the case of an unpaired electron residing in an orbital that is non-bonding with respect to the NO molecule.

Despite all these difficulties, an interpretation can be tried by comparison with the results of the parallel IR studies. In fact the behavior of the EPR spectra as a function of NO pressure (Fig. 16) shows a parallelism with the behavior observed by IR spectroscopy where the evolution of polynitrosyl complexes vs P_{NO} was observed. On the basis of this comparison we can assign the two observed EPR spectra to $Fe^{2+}(NO)_3$ and $Fe^{2+}(NO)$ species (Fig. 16, top and bottom spectra, respectively), both having nearly neutral NO ligands. The former compound should be written as $[-Fe(NO)_3]^{2+}$, with probably nine electrons in the d orbitals of the metal, while the latter should be $[Fe(NO)]^{2+}$, a true $[FeNO]^7$ compound according to the notation proposed by Enemark and Feltham (47). In this hypothesis the intense dinitrosyl species, clearly observed by IR, should correspond to an EPR-silent diamagnetic entity. Of course, this should be verified by means of *ad hoc* quantum calculations.

There is a remaining discrepancy between the IR and EPR data. In fact, while at high P_{NO} the EPR spectra indicate the total absence of $Fe^{2+}(NO)$ adducts, the IR spectra show that $Fe^{2+}(NO)$ species are still abundantly present (band at 1835 cm^{-1}; see above). This contradiction is only apparent if we consider the effect of clustering. In fact, if most of the Fe^{2+} ions forming $Fe^{2+}(NO)$ species absorbing at 1835 cm^{-1} are clustered, after adsorption of NO they are EPR silent because of dipolar interaction.

In conclusion, the EPR spectroscopy is informative about the $Fe^{2+}(NO) \rightarrow Fe^{2+}(NO)_3$ chemistry of isolated ions, while IR reveals also the relevant fraction of clustered Fe^{2+} forming bidimensional islands. This conclusion confirms that only a multitechnique analysis can give a reasonable picture of a complex catalytic system and, more important, that isolated and clustered surface species are simultaneously present even in highly diluted samples.

4.6. A Simplified Model of the Formation, Structure, and Distribution of Extraframework Iron Species

In Section 1 we briefly discussed how the method of the controlled migration of Fe from framework positions in Fe silicalite is far from being a simple and completely understood process, and we showed that many factors can influence the final structure and distribution of the potentially active species. On the basis of the complete set of data here discussed, we present a simplified dislodgment
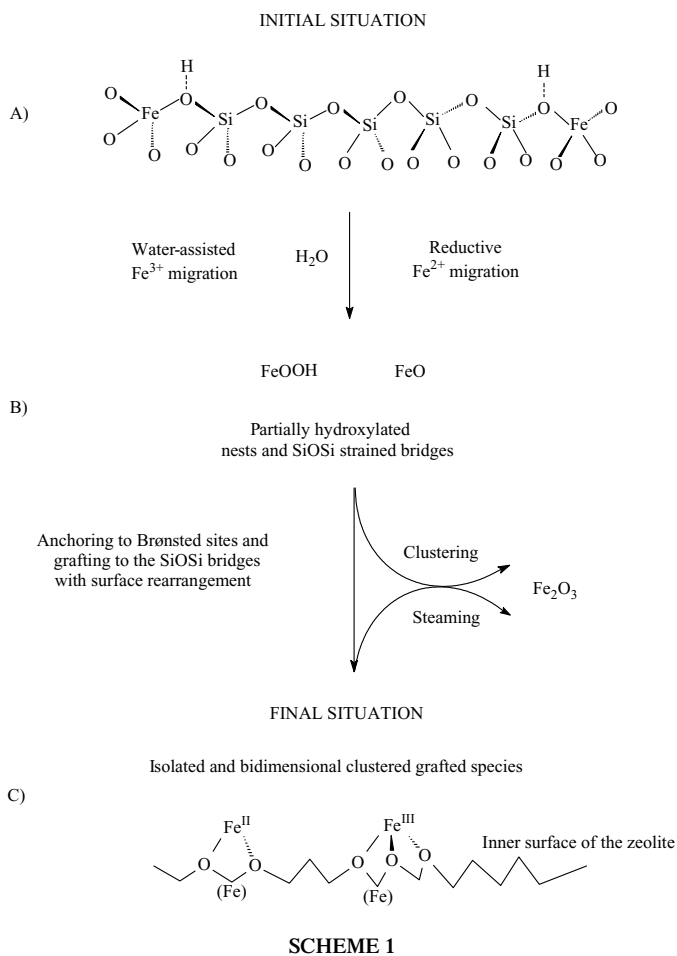
SCHEME 1

and migration pathway (Scheme 1) that explains the observed properties of the extraframework species described so far. The structure of Scheme 1, concerning the overall migration process, is based on the (partially consecutive) reaction steps described in Sections 4.6.1–4.6.4.

4.6.1. Water-catalyzed Fe^{3+} migration. The A $\rightarrow$ B evolution in Scheme 1 is based on the fact, widely documented for Al (3, 52), that the dislodgment of heteroatoms into extraframework positions in zeolites is assisted by traces of water. This hydrolysis reaction can favor the breaking of Si–O and Fe–O bonds, with the formation of new SiOSi and SiOFe bridges. We can assume that the dislodgment process is stepwise, each step being associated with the breaking of one SiOFe bridge and the formation of FeOH and SiOH pairs. This process can also be incomplete, giving rise to partially extraframework species. Thus, it can be inferred that the total migration of Fe into extraframework position produces nascent FeOOH species and partially hydroxylated nests or nanocavities. At high temperatures the former can eliminate water and form strained SiOSi bridges. Notice that strained SiOSi bridges can undergo a substantial annealing process (44).

4.6.2. Reductive Fe migration. XANES, IR, and EPR spectra indicate the formation of extraframework Fe^{2+} species. This evidence suggests that the dislodgment and migration of Fe^{3+} is accompanied by redox reactions leading to ferrous FeO and/or $Fe(OH)_2$ species (A → B in Scheme 1). The reduction process can be due either to spontaneous loss of oxygen at high temperatures or, although less likely, to the presence of hydrocarbons and other carbonaceous impurities (53), or to both. In samples characterized by a low concentration of iron species, hydrocarbon impurities can play some role in determining the final oxidation state of the dislodged species.

4.6.3. Reaction with the host matrix (residual Brønsted sites and/or zeolite walls). The B → C evolution in Scheme 1 is based on the hypothesis that the nascent extraframework species (FeOOH or FeO) can travel along the channels and react with (i) SiOH and strained SiOSi groups or (ii) residual Brønsted Si(OH)Fe sites. This results in (i) isolated or (ii) dimeric grafted species. Scheme 2 describes in detail suggestions for such reactions.

The relative concentration of the four species represented in Scheme 2 depends upon many factors. Traces of reducing/oxidizing agents can tune the 2a ↔ 2b and 2c ↔ 2d equilibria. All species can be mobile in the presence of traces of water so that isolated and dimeric grafted species can be in dynamical equilibrium. Structures 2a and 2b are similar to the partially extraframework species obtained in the stepwise dislodgment from T positions (Section 4.6.1). As a consequence, a dynamical equilibrium between totally and partially extraframework species should be considered.

The iron structures generated following reactions a–d in Scheme 2 are the $L_2N_n Fe^{2+}$ and $L_3N_m Fe^{3+}$ species invoked (Eqs. [2a]–[2c]) to explain the complex IR spectroscopy of adsorbed NO. The classification of the Fe species in terms of number and strength of ligands in the first coordination shell is appropriate for the description of the chemical properties of the sites toward probe molecules showing no bridging ability (like CO, NO, or N_2O). However, it fails in describing the properties toward oxygen, because O_2^{2-} or O^{2-} species can act as bridging ligands between Fe^{x+}-centers in adjacent positions (see Section 4.4.6).
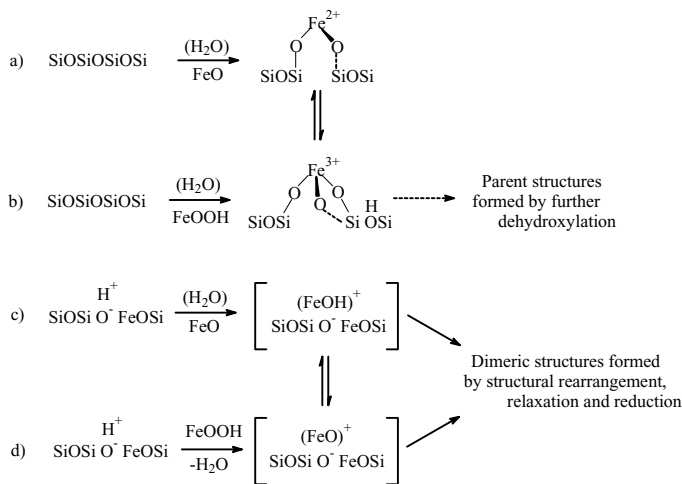
4.6.4. Clustering. The final clustering step represents an evolution of the previously described extraframework species. High-temperature treatments favor the mobility of all iron species. Partially extraframework species can migrate along the internal surface of the hosting matrix, generating islands of grafted species which can be considered bidimensional clusters (Scheme 1C). As for the fully extraframework FeOOH and FeO species which have not reacted with the walls sites, they can lead to $(Fe_2O_3)_n$, $(Fe_3O_4)_n$, and $(FeO)_n$ three-dimensional nanoparticles (Scheme 1B). High-nuclearity species could be favored under classical steaming conditions (54) and at the highest iron loading.

5. CONCLUSIONS

IR, XANES, and EPR have given useful information even on very diluted samples characterized by Si/Fe = 90 (XANES, IR) and Si/Fe = 150 (IR, EPR), i.e., on the "true" catalysts of partial oxidation reactions. Concerning the oxidation, coordination, and aggregation state of iron, the following picture emerged. (i) Migration of iron from the framework is accompanied by a $Fe^{3+} \rightarrow Fe^{2+}$ reduction. (ii) Both isolated and bidimensional clustered grafted Fe species are present. These species can be in mutual equilibrium at high temperatures in the presence of traces of water. (iii) Present as well are three-dimensional aggregates, whose concentration grows with Fe loading. These species do not adsorb CO, N_2O, or NO. Consequently, they are silent "inactive" guests. (iv) Fe^{3+} and Fe^{2+} isolated species which are in mutual equilibrium were detected, their relative concentration being dependent upon the length of the thermal treatment and upon the presence of reducing/oxidizing agents.

Fe^{2+} species showed a high heterogeneity and were classified as belonging to three main families characterized by their degree of coordinative unsaturation. They have been labeled $L_2N_n Fe^{2+}$, where L is a framework SiO^- (or atomic O^{2-}) chemically linked group and N is a framework oxygen atom of the vicinal SiOSi bridges electrostatically linked. Depending upon the number of N ligands (3, 2, or 1), the Fe^{2+} species can adsorb one, two, or three NO molecules with formation of well-defined nitrosyl species. Clustered Fe^{2+} species are all of the $L_2N_3 Fe^{2+}$ type and are thus able to adsorb only one NO molecule.

As far as oxidation treatments are concerned, EXAFS has shown the addition of oxygen in the coordination sphere of extraframework iron, while XANES has shown

a) SiOSiOSiOSi $\xrightarrow[\text{FeO}]{\text{(H}_2\text{O)}}$ [structure: Fe^{2+}, O, O, SiOSi, SiOSi]

b) SiOSiOSiOSi $\xrightarrow[\text{FeOOH}]{\text{(H}_2\text{O)}}$ [structure: Fe^{3+}, O, O, O, H, SiOSi, Si OSi] ----- Parent structures formed by further dehydroxylation

c) $\overset{H^+}{SiOSi\ O^-\ FeOSi}$ $\xrightarrow[\text{FeO}]{\text{(H}_2\text{O)}}$ $\left[(FeOH)^+ \atop SiOSi\ O^-\ FeOSi \right]$

d) $\overset{H^+}{SiOSi\ O^-\ FeOSi}$ $\xrightarrow[\text{-H}_2\text{O}]{\text{FeOOH}}$ $\left[(FeO)^+ \atop SiOSi\ O^-\ FeOSi \right]$

Dimeric structures formed by structural rearrangement, relaxation and reduction

SCHEME 2

that a large fraction of the extraframework Fe^{2+} species is oxidized to Fe^{3+}. IR results have shown that, while both isolated and clustered Fe^{2+} species are oxidized at 523 K, clustered species of the $L_2N_3Fe^{2+}$ type are preferentially affected after interaction with O_2 at room temperature. EPR results support the $Fe^{2+} \rightarrow Fe^{3+}$ transformation upon oxidation with O_2 and N_2O at high temperature.

Although these data are only indirectly related to the state of adsorbed oxygen, they support the following picture. Isolated as well as clustered species grafted onto the internal surface of the MFI channels and cavities can adsorb oxygen. Clustered Fe^{2+} species can form $Fe^{3+}\cdots O^{2-}\cdots Fe^{3+}$ or $Fe^{3+}\cdots O_2^{2-}\cdots Fe^{3+}$ groups already at low temperature. The oxygen species bridged on couple of Fe^{3+} ions can be easily removed by reducing agents. Isolated Fe^{2+} species only adsorb oxygen at higher temperature. The species formed upon oxidation of isolated Fe^{2+} species (presumably FeO^{2+}) can be transformed back into Fe^{2+} by thermal activation *in vacuo* or by contact with reducing agents. One of these two species might then correspond to the α-oxygen species proposed by Sobolev *et al.* (16).

REFERENCES

1. Szostak, R., and Thomas, T. L., *J. Catal.* **100**, 555 (1986).
2. Bordiga, S., Buzzoni, R., Geobaldo, F., Lamberti, C., Giamello, E., Zecchina, A., Leofanti, G., Petrini, G., Tozzola, G., and Vlaic, G., *J. Catal.* **158**, 486 (1996).
3. Jacobs, P. A., and Beyer, H. K., *J. Phys. Chem.* **83**, 1174 (1979).
4. Gubelmann, M., and Tirel, P.-J., Fr. Patent 2,630,735 (1988).
5. Kharitonov, A. S., Alexandrova, T. N. L., Vostrikova, A., Ione, K. G., and Panov, G. I., Russ. Patent 4,445,646 (1988).
6. Feng, X., and Hall, W. K., *J. Catal.* **166**, 368 (1997).
7. Dubkov, A., Ovanesyan, N. S., Shteinman, A. A., Dubkov, K. A., Sobolev, V. I., and Panov, G. I., *Kinet. K catal.* **39**, 792 (1998).
8. Chen, H.-Y., and Sachtler, W. M. H., *Catal. Today* **42**, 73 (1998).
9. Joyner, R., and Stockenhuber, M., *J. Phys. Chem. B* **103**, 5963 (1999).
10. Kögel, M., Mönning, R., Schwieger, W., Tissler, A., and Turek, T., *J. Catal.* **182**, 470 (1999).
11. Marturano, P., Kogelbauer, A., and Prins P., *J. Catal.* **190**, 460 (2000).
12. Marturano, P., Drozdová, L., Kogelbauer, A., and Prins, R., *J. Catal.* **192**, 236 (2000).
13. Chen, H.-Y., El-Malki, El-M., Wang, X., van Santen, R. A., and Sachtler, W. M. H., *J. Mol. Catal. A* **162**, 159 (2000).
14. Fejes, P., Nagy, J. B., Halász, J., and Oszkó, A., *Appl. Catal.* **61**, 85 (1990).
15. Ribera, A., Arends, I. W. C. E., de Vries, S., Pérez-Ramírez, J., and Sheldon, R. A., *J. Catal.* **195**, 287 (2000).
16. Sobolev, V. I., Panov, G. I., Kharitonov, A. S., Romannikov, V. N., Volodin, A. M., and Ione, K. G., *J. Catal.* **139**, 435 (1993).
17. Lewis, D. W., Catlow, R. A., Sankar, J., and Carr, S. W., *J. Phys. Chem.* **99**, 2377 (1995).
18. Spoto, G., Zecchina, A., Berlier, G., Bordiga, S., Clerici, M. G., and Basini, L., *J. Mol. Catal. A* **158**, 107 (2000).
19. Axon, S. A., Fox, K. K., Carr, S. W., and Klinowski, J., *Chem. Phys. Lett.* **189**, 1 (1992).
20. Suzuki, E., Nakashiro, K., and Ono, Y., *Chem. Lett.* 953 (1998).
21. Notté, P. P., *Top. Catal.* **13**, 387 (2000).
22. Franz, K. J., and Lippard, S. J., *J. Am. Chem. Soc.* **121**, 10504 (1999).
23. Delgass, W. N., Garten, R. L., and Boudart, M., *J. Phys. Chem.* **73**, 2970 (1969).
24. Jermyn, J. W., Johnson, T. J., Vansant, E. F., and Lunsford, J. H., *J. Phys. Chem.* **77**, 2964 (1973).
25. Aparicio, L. M., Hall, W. K., Fang, S.-M., Ulla, M. A., Millman, W. S., and Dumesic, J. A., *J. Catal.* **108**, 233 (1987).
26. Lobree, L. J., Hwang, I.-C., Reimer, J. A., and Bell, A. T., *J. Catal.* **186**, 242 (1999).
27. Szostak, R., Nair, V., and Thomas, T. L., *J. Chem. Soc. Faraday Trans. 1* **83**, 487 (1987).
28. Ratnasamy, P., and Kumar, R., *Catal. Today* **9**, 329 (1991).
29. Lytle, F. W., Sayers, D. E., and Stern, E. A., *Physica B* **158**, 701 (1989).
30. Michalowicz, A., *J. Phys. IV* **7**, C2-235 (1997).
31. McKale, A. G., Veal, B. W., Paulikas, P. A., Chan, S. K., and Knapp, G., *J. Am. Chem. Soc.* **110**, 3763 (1988).
32. Zecchina, A., Geobaldo, F., Lamberti, C., Bordiga, S., Turnes Palomino, G., and Otero Areán, C., *Catal. Lett.* **42**, 25 (1996).
33. Lamberti, C., Turnes Palomino, G., Bordiga, S., Zecchina, A., Spanò, G., and Otero Areán, C., *Catal. Lett.* **63**, 213 (1999).
34. Bianconi, A., *in* "X-Ray Absorption" (D. C. Koningsberger and R. Prins, Eds.), p. 573. Wiley, New York, 1988.
35. Long, G. J., Cheetham, A. K., and Battle, P. D., *Inorg. Chem.* **22**, 3012 (1983).
36. Pang, L., Hynes, R. C., and Whitehead, M. A., *Acta Crystallogr. C* **48**, 1594 (1992).
37. Sawada, H., *Mater. Res. Bull.* **31**, 141 (1996).
38. Bordiga, S., Escalona Platero, E., Otero Areán, C., Lamberti, C., and Zecchina, A., *J. Catal.* **137**, 179 (1992).
39. Zecchina, A., Scarano, D., Bordiga, S., Spoto, G., and Lamberti, C., *Adv. Catal.* **46**, 265 (2001).
40. Zecchina, A., Bordiga, S., Spoto, G., Marchese, L., Petrini, G., Leofanti, G., and Padovan, M., *J. Phys. Chem.* **96**, 4985 (1992).
41. Spoto, G., Bordiga, S., Garrone, E., Ghiotti, G., and Zecchina, A., *J. Mol. Catal.* **74**, 175 (1992).
42. Busca, G., and Lorenzelli, V., *J. Catal.* **72**, 303 (1981).
43. Bohle, D. S., and Hung C.-H., *J. Am. Chem. Soc.* **117**, 9584 (1995).
44. Bordiga, S., Ugliengo, P., Damin, A., Lamberti, C., Spoto, G., Zecchina, A., Spanò, G., Buzzoni, R., Dalloro, L., and Rivetti, F., *Top. Catal.* **15**, 43 (2001).
45. Goldfarb, D., Bernardo, M., Strohmaier, D., Vaughan, D. E. W., and Thomann, H., *J. Am. Chem. Soc.* **116**, 6344 (1994).
46. Goldfarb, D., Strohmaier, D., Vaughan, D. E. W., Thomann, H., Poluektov, O. G., and Schmidt, J., *J. Am. Chem. Soc.* **118**, 4665 (1996).
47. Enemark, J. H., and Feltham, R. D., *Coord. Chem. Rev.* **13**, 339 (1974).
48. Wescott, B. L., and Enemark J. H., *in* "Inorganic Electronic Structure and Spectroscopy" (E. Solomon and A. B. P. Lever, Eds.), Vol. 2, p. 403. Wiley, New York, 1999.
49. Wu, Z., Xian, D. C., Natoli, C. R., Marcelli, A., Paris, E., and Mottana, A., *Appl. Phys. Lett.* **79**, 1918 (2001).
50. Volodin, A. M., Dubkov, K. A., and Lund, A., *Chem. Phys. Lett.* **333**, 41 (2001).
51. Mingos, D. M. P., and Sherman, D. J., *Adv. Inorg. Chem.* **34**, 293 (1979).
52. Wouters, B. H., Chen, T.-H., and Grobet, P. J., *J. Am. Chem. Soc.* **44**, 11419 (1998).
53. Dossi, C., Fusi, A., Moretti, G., Recchia, S., and Psaro, R., *Appl. Catal. A* **188**, 107 (1999).
54. Ferretti, A. M., Oliva, C., Forni, L., Berlier, G., Zecchina, A., and Lamberti, C., *J. Catal.* **208**, 83 (2002).